JOURNAL OF GEOPHYSICAL RESEARCH, VOL. 114, B03401, doi:10.1029/2008JB005653, 2009

Volcano load control on dyke propagation and vent distribution: Insights from analogue modeling

M. Kervyn,[1] G. G. J. Ernst,[1] B. van Wyk de Vries,[2] L. Mathieu,[2,3] and P. Jacobs[1]

Received 25 February 2008; revised 17 December 2008; accepted 9 January 2009; published 3 March 2009.

[1] The spatial distribution of eruptive vents around volcanoes can be complex and evolve as a volcano grows. Observations of vent distribution at contrasting volcanoes, from scoria cones to large shields, show that peripheral eruptive vents concentrate close to the volcano base. We use analogue experiments to explore the control of volcano load on magma ascent and on vent location. Results show that the local loading stress field favors eruption of rising magma away from the volcano summit if a central conduit is not established or is blocked. Two sets of scaled experiments are developed with contrasting rheological properties to analyze similarities and differences in simulated magma rise below a volcano: (1) Golden syrup (magma analogue) is injected into a sand-plaster mixed layer (crust analogue) under a cone; (2) water or air (magma analogues) is injected into gelatin under a sand cone. Rising dykes approaching the cone stress field are stopped by the load compressive stress. With continued intrusion, dyke overpressure builds up; dykes extend laterally until their tips are able to rise vertically again and to erupt in the flank or at the base of the volcano. Lateral offset of the extrusion point relative to the edifice summit depends on substratum thickness, volcano slope, and dyke overpressure. The 3D geometry of Golden syrup intrusions varies with experimental parameters from cylindrical conduits to dyke and sill complexes. Experimental results are compared with illustrative field cases and with previously published numerical models. This comparison enables applications and limitations of the analogue models to be highlighted and allows us to propose a conceptual model for the evolution of vent distribution with volcano growth.

Citation: Kervyn, M., G. G. J. Ernst, B. van Wyk de Vries, L. Mathieu, and P. Jacobs (2009), Volcano load control on dyke propagation and vent distribution: Insights from analogue modeling, *J. Geophys. Res.*, *114*, B03401, doi:10.1029/2008JB005653.

1. Introduction

[2] A volcano grows by successive eruptions from a central vent and/or from vents on the flanks or around the base. It can also grow endogenously by intrusion. Intrusions contribute to edifice construction in a complex way. They can add volume [*Annen et al.*, 2001], raise slopes, alter load distribution or cause spreading and collapse. Also, they can deform edifices, changing the stress distribution, and thus the boundary conditions for future intrusions and ultimately eruptions [e.g., *Walter and Amelung*, 2006].

[3] The distribution of peripheral vents can be complex and evolve through time. It is controlled by interaction of regional and local factors: i.e., regional and local stress fields, regional structures, volcano shape, spreading structures and direction, magma chamber location and size, magma composition [e.g., *Bacon*, 1985; *Connor et al.*, 1992; *Fialko and Rubin*, 1999; *Mazzarini and D'Orazio*, 2003; *Corazzato and Tibaldi*, 2006]. Vent distribution in turn influences volcano growth and morphology. Documenting and identifying factors controlling vent distribution can provide insights into controls on magma plumbing.

[4] It is common to find peripheral vents or to observe eruptions focusing close to a volcano base or at a marked break-in-slope (BIS) on the lower flanks [e.g., *Poland et al.*, 2008]. The relationship between topography and vent location can be documented at many volcanoes using remote sensing topographic data. However, the process leading to preferential vent opening away from the volcano summit and close to its base has been little discussed [*Shteynberg and Solovyev*, 1976; *Fialko and Rubin*, 1999; *Pinel and Jaupart*, 2004b; *Gaffney and Damjanac*, 2006].

[5] Numerous dynamic models for dyke (i.e., liquid-filled fracture) propagation assuming a homogeneous half-space have been proposed [*Johnson*, 1970; *Pollard*, 1973, 1987; *Dahm*, 2000; *Menand and Tait*, 2002, and references therein]. It has been proposed that dyke propagation direction is mainly controlled by regional stress orientation, presence of planar discontinuities in the host rock, or

---

[1] Mercator and Ortelius Research Centre for Eruption Dynamics, Department of Geology and Soil Sciences, Ghent University, Gent, Belgium.

[2] Laboratoire Magma et Volcans, Université Blaise Pascal, Clermont-Ferrand, France.

[3] Volcanic and Magmatic Processes Research Group, Trinity College Dublin, Dublin, Ireland.

0148-0227/09/2008JB005653$09.00

changes in host rock rheological properties [e.g., *Pollard*, 1973]. Dyke propagation in the crust or within volcanic constructs has also been studied with analogue modeling, using liquid injection into gelatin [*Pollard*, 1973; *Hyndman and Alt*, 1987; *Menand and Tait*, 2002; *Kavanagh et al.*, 2006; *Rivalta and Dahm*, 2006, and references therein]. Some field studies are available to evaluate results from numerical and experimental models [*Walker*, 1993, 1995, 1999; *Gudmundsson*, 2002; *Klausen*, 2006; *Poland et al.*, 2008]. However, the 2D nature of field outcrops limits the ability to reconstruct the 3D shape of subvolcanic intrusions. 3D seismic observations has recently shown some new insights into the complex shape of intrusive bodies, but with limited success for dykes [e.g., *Thomson*, 2007].

[6] Some work has been dedicated to the propagation of dykes approaching volcanic constructs. *Pinel and Jaupart* [2000, 2004b] developed a 2D numerical model predicting that ascending dykes can be blocked underneath high volcanoes (i.e., cone height ~4 km for shields and ~2 km for stratovolcanoes). Edifice load causes magma storage at depth, or, if magma is of sufficiently low density, it favors lateral dyke propagation and extrusion at the volcano base. *Gaffney and Damjanac* [2006] numerically modeled effects from topography on a dyke rising under a ridge adjacent to a lowland. In this model, dykes tend to erupt in lower areas, mostly because of the geometric effect of topography and, to a lesser extent, to the lateral confining stresses from the ridge. These model predictions have not yet been evaluated experimentally. In this paper, experimental results are presented to evaluate the hypothesis that edifice load affects magma ascent as well as vent outbreak spatial distribution.

[7] Previous gelatin models have documented that stress field reorientation from surface loading (i.e., presence of a volcano) causes focusing of ascending dykes below the load axial zone [*Dahm*, 2000; *Muller et al.*, 2001; *Watanabe et al.*, 2002]. Using injection of hot gelatin into a gelatin block overlain by a gelatin cone, *Hyndman and Alt* [1987] observed that as dykes approached the volcano base, they extended laterally, although this process was not fully documented or discussed. Within cones, dykes have also been observed to reorientate locally perpendicular to topographic contours [*McGuire and Pullen*, 1989] and to reorientate parallel to the headwalls of a collapse scar [*Walter and Troll*, 2003].

[8] Here, two types of experiments were designed to investigate the volcano load control upon dyke ascent trajectory and upon dyke surface outbreak's location. Dyke propagation below a volcanic cone is modeled by injecting: (1) Golden syrup into fine granular material and (2) water or air into gelatin. These analogue models simulate some key dynamic aspects of magma ascent in a continuous (mostly isotropic) medium. Using two media of contrasting rheological properties enables simulation of two fundamentally different processes leading to dyke propagation, i.e., shear failure versus tensional hydraulic fracturing, thought to be the dominant dyke propagation mechanisms in granular and gelatin media, respectively (see the work of *Mathieu et al.* [2008] for discussion). Experiments in the granular media enable documentation of both the 3D morphology of subvolcanic intrusions and the associated surface deformation. The present study builds closely upon analogue modeling of dyke ascent through a brittle crust toward a flat surface [*Mathieu et al.*, 2008]. Here the main difference is that the effect of edifice load is now considered.

[9] To predict propagation and outbreak location before a dyke reaches the surface, it is important to understand processes controlling dyke initiation, propagation in the crust or within a volcanic edifice, and interaction with the surrounding rock. The objective of this paper is to illustrate and analyze volcano load control upon dyke ascent in the upper crust and upon outbreak location. Experiments simulate dykes ascending from a deep source, below a homogenous circular cone without any pre-established structure (e.g., conduit, rift zone, dyke swarm) controlling magma propagation. Attention is paid to scaling experiments for basalt/andesite magma viscosity, but we expect results to be valid for a wider viscosity range.

2. Vent Concentration at a Volcano Base

2.1. Stratocones and Long-Lasting Scoria Cones

[10] The geological evolution and vent distribution at Concepción, Nicaragua, is presented by *van Wyk de Vries* [1993] and *Borgia and van Wyk de Vries* [2003]. This typical stratovolcano is mostly built through central eruptions, but about 20 peripheral vents (e.g., scoria cones, tuff rings and lava domes) are located between 2.5 and 7 km from the summit (Figure 1). Peripheral vents to the E and W are associated with relatively early stages of volcano growth. They are located on flat terrains, at 200–400 m a.s.l., in association with a circular topographic rise around the volcano base, interpreted to be a structure caused by volcano flexure. Other peripheral vents are located on the lower flanks (i.e., slope <15°) along a N–S structure related to more recent volcano spreading [*Borgia and van Wyk de Vries*, 2003].

[11] The base of steep flanks is identified as a preferential location for vents at other steep conical volcanoes; e.g., at Arenal, Costa Rica [*Borgia et al.*, 1988], and Mount Adams, USA [*Hildreth and Fierstein*, 1997]. Seven of the ten Holocene vents at Mount Adams are located within 2 km below the break-in-slope (BIS) between the steep rubbly cone and less steep flank lava apron. At Arenal and Mount Adams, BIS vent concentration is attributed to a lithological contrast [*Borgia et al.*, 1988; *Hildreth and Fierstein*, 1997]. Even where tectonic stresses control vent localization, peripheral vents are found away from the summit beyond the point where slope gradient starts to decrease rapidly: e.g., Navidad cone 1989 eruption at Lonquimay, Chile [*Naranjo et al.*, 1992]; Nasira cones at Oldoinyo Lengai, Tanzania [*Kervyn et al.*, 2008].

[12] Young stratovolcanoes (e.g., Cerro Negro, Nicaragua, Figure 2; Izalco, El Salvador [*Carr and Pontier*, 1981]), or scoria cones with long-lasting (Parícutin, Mexico: 1943–1951 [*Luhr and Simkin*, 1993]) or repetitive eruptions (Etna SE cone, Italy [e.g., *Behncke et al.*, 2006]), also have vents opening at the edifice base, even though these constructs were built mostly from eruptions through a central conduit. At Parícutin vents opened at distinct points along the original fissure, but also at the cone base, often when the central conduit was inactive or blocked. At Cerro Negro, there have been repeated lava extrusions or secondary cone-building vents at the cone base which is defined by a rapid decrease in slope angle from >20° to <15° within 200 m. (Figure 2).

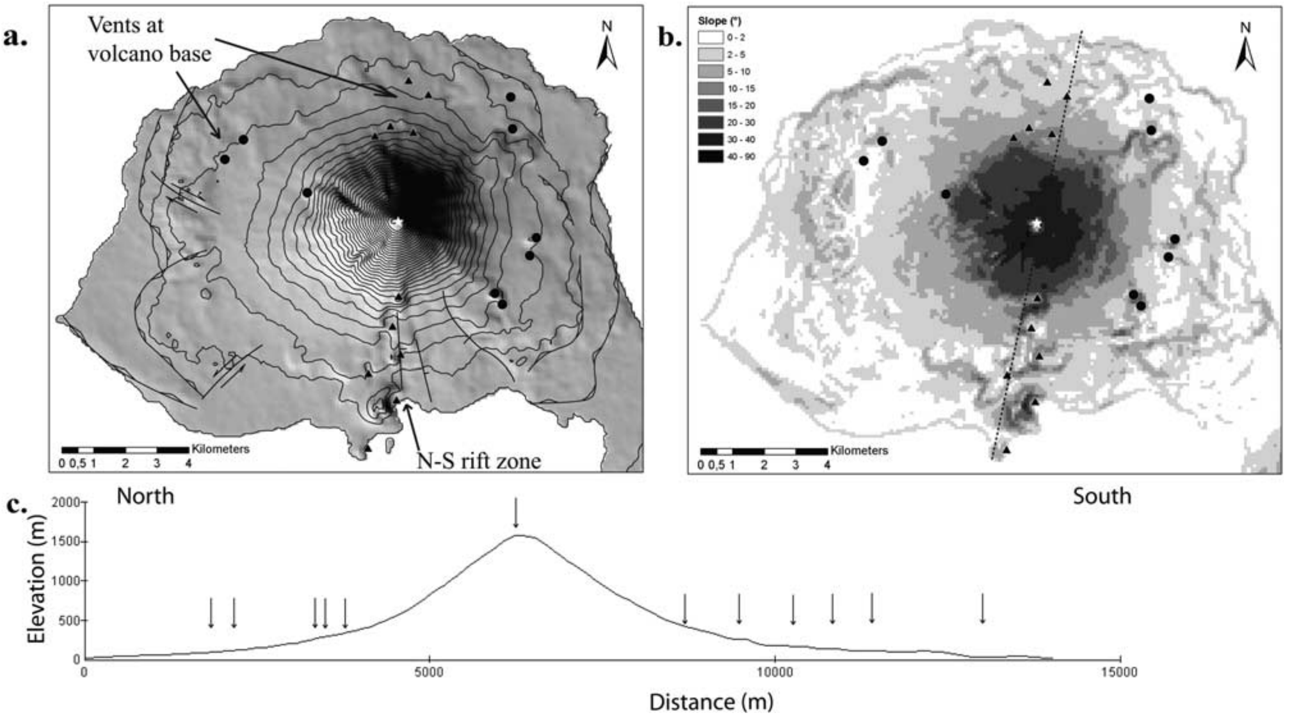

Figure 1. Vent distribution at Concepción volcano, Nicaragua. (a) Shaded relief and structural features; (b) slope angle; (c) north–south topographic profile along dashed line in Figure 1b. Arrows indicate the location of vents, including several at the cone base. Old domes (circles) and Holocene cones (triangles) along a pronounced north–south rift zone are all located on the lower volcano slopes (adapted from the works of *van Wyk de Vries* [1993] and *Borgia and van Wyk de Vries* [2003]).

[13] The 2000 seismic/volcanic crisis at Miyakejima, Japan, also provided evidence for preferential dyke outbreak at the volcano base [*Kaneko et al.*, 2005]. The first eruption stage was a lateral dyke intrusion causing an earthquake swarm propagating 30 km from Miyakejima. The dyke breached the surface at the volcano base, causing a submarine eruption [*Kaneko et al.*, 2005]. A similar lateral dyke injection associated with peripheral eruption and central caldera subsidence was also inferred for the 1912 Novarupta (Katmai) eruption [*Hildreth and Fierstein*, 2000].

2.2. Shield Volcanoes

[14] The large oceanic Galapagos shields (e.g., Fernandina, Cerro Azul) display an illustrative vent distribution related to topography [e.g., *Chadwick and Dietrich*, 1995; *Naumann and Geist*, 2000]. Vents are arranged in a circumferential pattern on a summit plateau (i.e., along the caldera rim). They are fed by gas-rich magma and produce short tube-fed pahoehoe flows at low eruption rates. At the break-in-slope between the steep upper flanks (>15°) and more gentle lower flanks (<10°), vents are radially oriented. They are fed by gas-poor or degassed magma and produce voluminous aa flows [*Naumann and Geist*, 2000]. Coexistence of circumferential fissures around the caldera rim and radial fissures lower on the flanks was attributed to a diapiric-shaped magma chamber and to edifice load by *Chadwick and Dietrich* [1995].

2.3. Late-Stage Shields

[15] The vent distribution at Mauna Kea, Hawaii (USA), is also illustrative of vent concentration at the BIS. Vent distribution at actively growing Hawaiian shields is mostly limited to well-defined rift zones (e.g., Kilauea, Mauna Loa) as dykes intrude laterally from a shallow magma reservoir [*Decker*, 1987; *Walker*, 1990, 1999]. The end of shield building is marked by a decrease in magma supply rate and by cooling of the high-level magma chamber [*Moore and Clague*, 1992] only allowing eruptions of small, separate magma batches. This results in a scatter of 300 vents on the flanks and at the base of Mauna Kea's upper steep flanks (Figure 3) [*Mac Donald*, 1945; *Porter*, 1972]. About half of these vents are located within 3 broad and short rift zones in the W, NE and SSE upper steep flanks. 40% of the vents, outside or within rift zones, are located at or beyond the base of the steep upper flanks, where slopes change abruptly from >15° to <10°. This is especially well illustrated by a high concentration of vents at the N base of the upper flank (Figure 3). Examples of 1–2-km-long vent alignments (3–4 vents) originating at the break-in-slope and extending outward are also found to the SW and ESE. Similarly, at other steep shields such as Mount Etna (Italy) or Nyiragongo (DRCongo), vents outside rift zones are found within 1 km from the base of steep upper flanks.

[16] As observed around the Dolomieu cone at Piton de la Fournaise (Réunion Island, France), BIS vent constructs tend to be larger than upper flank vents. Lower elevation lava eruptions are also typically larger in volume than those occurring from fissures at the top or along the upper flank (e.g., Mount Cameroon [*Suh et al.*, 2003]; Piton de la Fournaise [*Battaglia et al.*, 2005]).

[17] Topography is not the only control upon vent location and vents can be spread widely at a volcano. The above

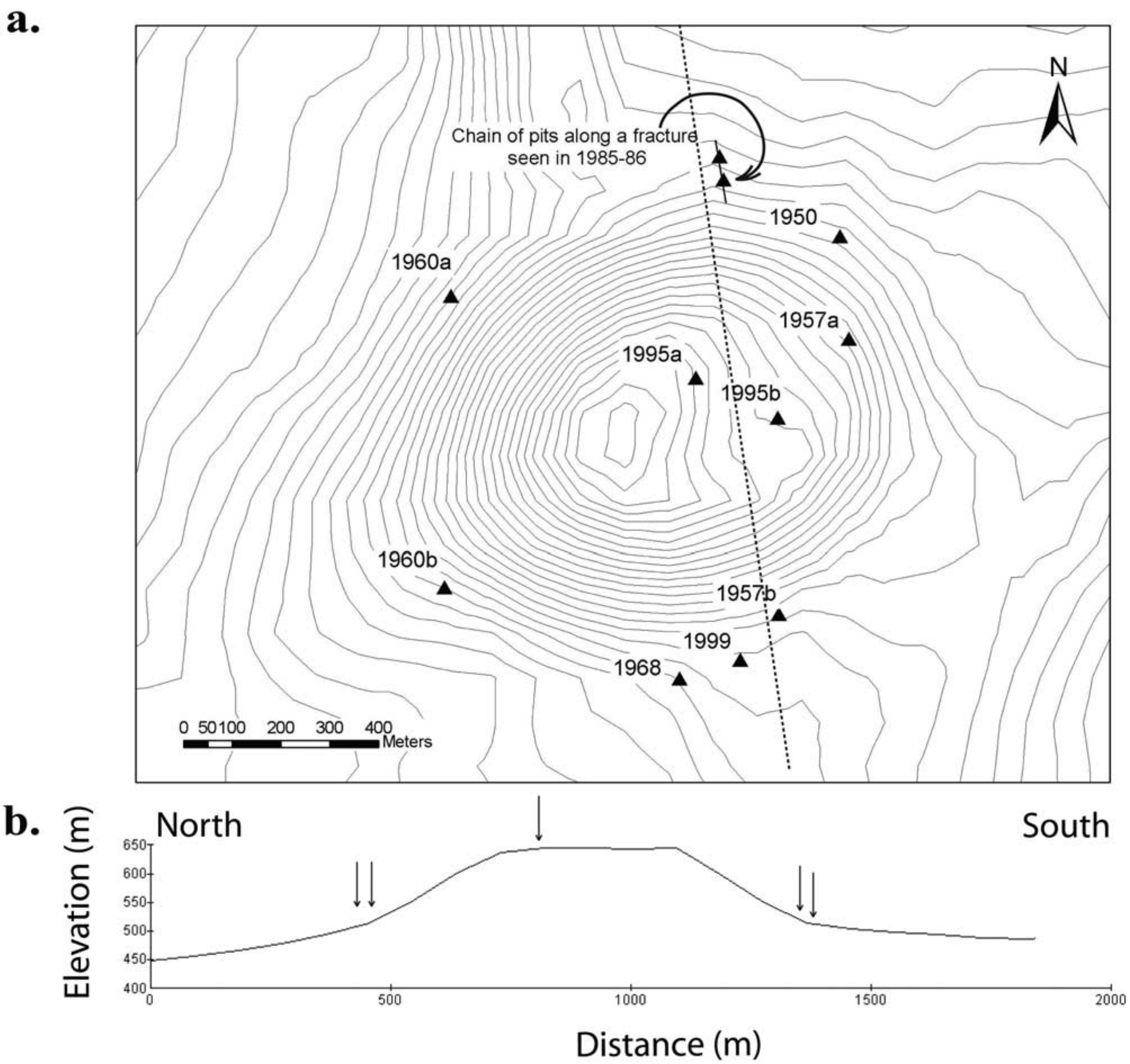

Figure 2. Vent distribution at Cerro Negro, Nicaragua. (a) Contour lines (10 m) with location of vents from recent eruptions (adapted from the work of *McNight* [1995]); (b) north–south topographic profile along dashed line in Figure 2a. Arrows indicate the location of vents, including several at the cone base.

examples however highlight that peripheral vents are often found far away from the volcano summit, beyond the transition from steep upper flanks to more gently sloping lower flanks. Similar examples can be found from many other Holocene or historically active volcanoes [*Simkin and Siebert*, 1994] with diverse shapes and sizes. Although we do not argue that the same processes of dyke propagation act in the same way at these different scales, these observations suggest that the local stress field directly below and within volcanic edifices favors dyke propagation away from the volcano summit (Figure 4). This is investigated and evaluated with the analogue models presented hereafter. It should be noted that the change in slope gradient can often be attributed to a different types of: (1) volcanic deposits (i.e., pyroclastics versus lava) or (2) deposition dynamics (i.e., flow versus fallout). This implies that the topographic BIS is often associated with a lithological boundary that can also affect dyke propagation. In order to isolate the effect of edifice loading from purely lithological effects, the litho-

Figure 3. Vent distribution at Mauna Kea, Hawaii. (a) Slope map; (b) map of the second derivative of the elevation at 750-m spatial resolution, highlighting with darker colors the places with rapid changes in slope angle; (c) north–south topographic profile along dashed line in Figure 3b. Arrows indicate the location of vents, including several at the cone base. In addition to 3 rift zones, vents are located at the base of the steep upper flanks and further downslope (within ellipses in Figure 3a).

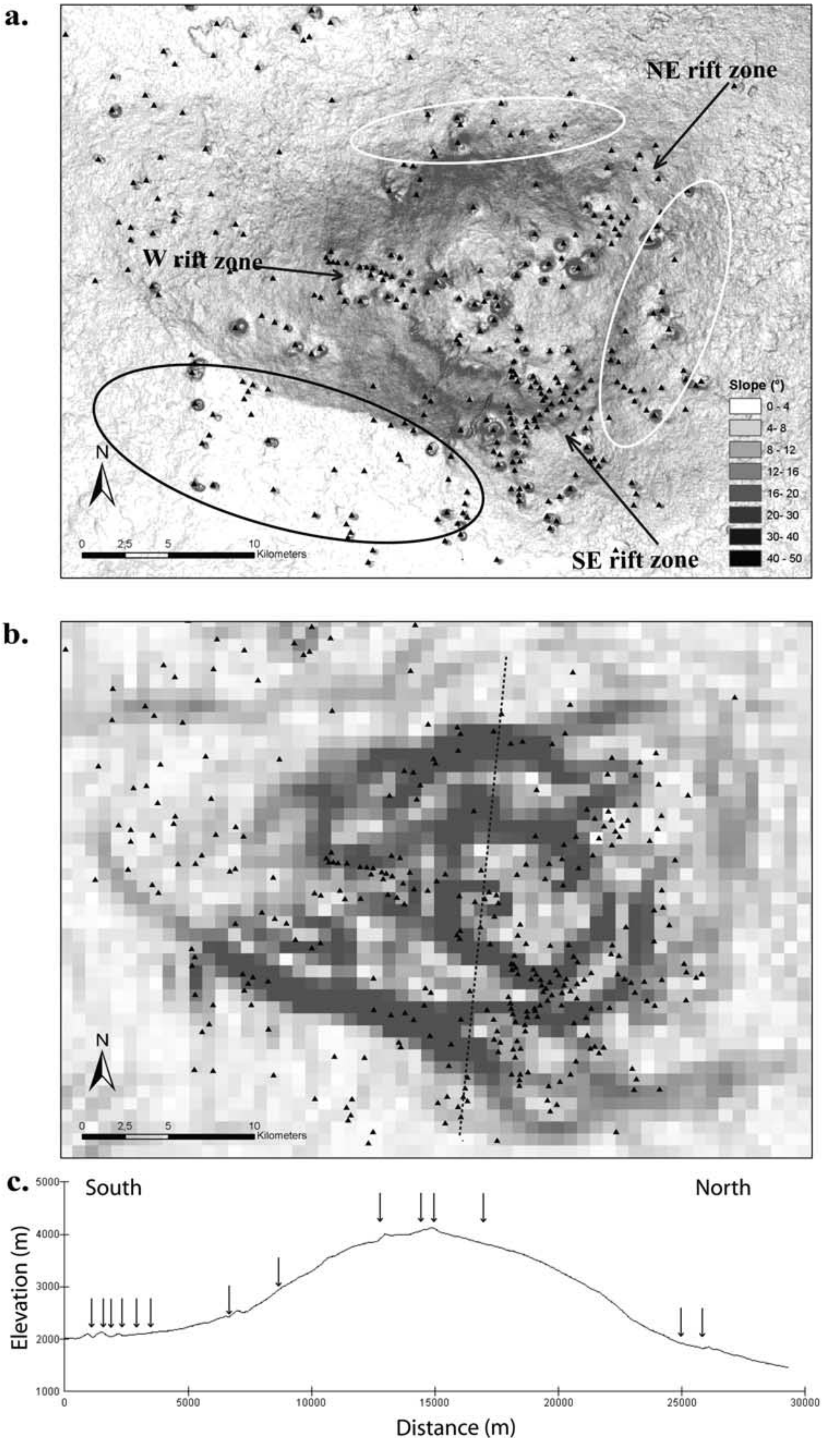
a.
NE rift zone
W rift zone
SE rift zone
Slope (°)
0 - 4
4 - 8
8 - 12
12- 16
16- 20
20- 30
30- 40
40 - 50
N
0 2,5 5 10 Kilometers
b.
N
0 2,5 5 10 Kilometers
c.
South
North
Elevation (m)
1000
2000
3000
4000
5000
0
5000
10000
15000
20000
25000
30000
Distance (m)

Figure 3

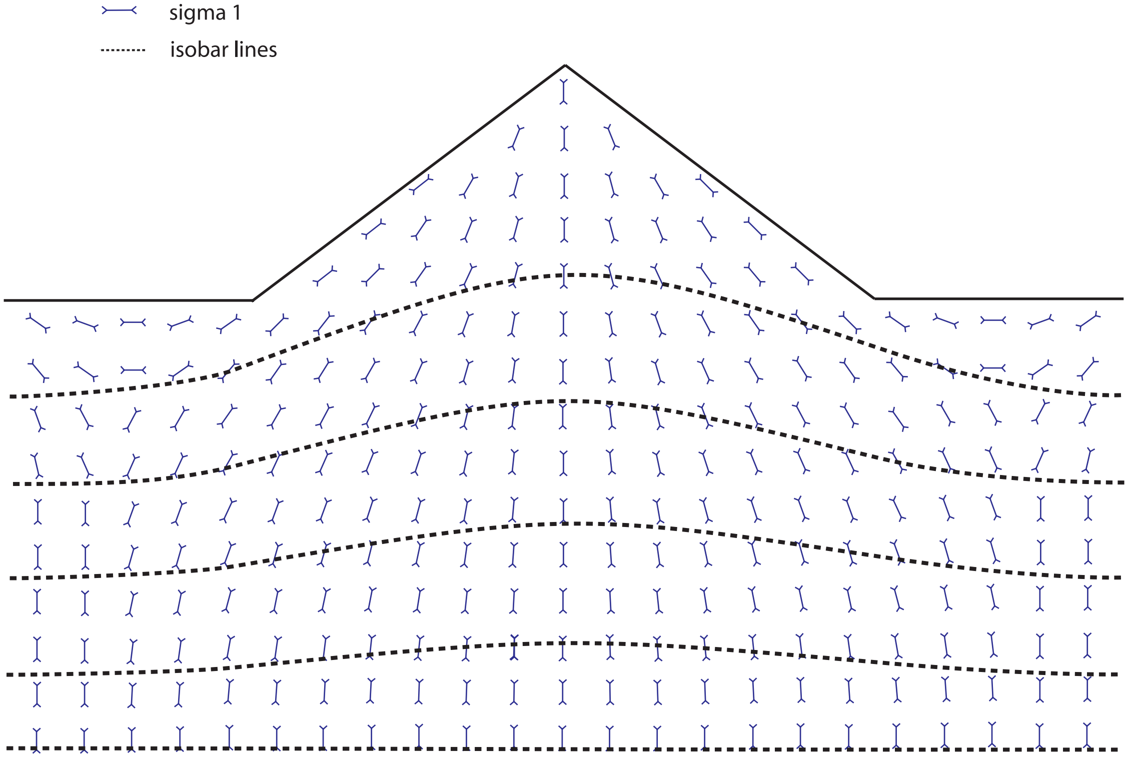

Figure 4. Conceptual representation of the σ_1 orientation and of the isobar lines in the substratum and in a volcanic cone based on *Dieterich* [1988] and *van Wyk de Vries and Matela* [1998]. Dykes would generally propagate perpendicularly to the least principal stress and parallel to orientations of σ_1 and σ_2. The stress distribution within a conical edifice will tend to focus dykes toward the central axis. On the other hand, the pressure gradient below the volcano's load can favor lateral dyke propagation toward lower confining pressure so that dykes would tend to migrate out from under the volcano [*van Wyk de Vries*, 1993].

logical boundary is not simulated in the presented analogue models.

3. Dyke Propagation in Granular Material

3.1. Analogue Materials and Scaling

[18] Fine granular material (i.e., a sand and plaster mixture) was used as analogue for upper crust country rocks and for the volcanic cone. Golden syrup (GS) at room temperature (20–25°C) was used as magma analogue. For similarity between the model and nature, the geometric, dynamic, and time parameters of the model (Table 1) must be scaled [*Ramberg*, 1981; *Merle and Borgia*, 1996; *Donnadieu and Merle*, 1998]. At the volcano scale, as an approximation, the stress ratio between nature and models, σ^*, can be estimated from

$$\sigma^* = \rho^* \times g^* \times h^* \qquad (1)$$

where ρ^*, g* and h* are the model/nature ratios for the density, gravitational acceleration, and height of the volcanic cone, respectively. This calculation yields a stress ratio of $\sim 10^{-6}$–10^{-4} (Table 1). Hence an analogue volcano should be 10^4–10^6 times mechanically weaker than a real volcano. A mixture of sand ($\sim$250 μm median grain size) with 30 wt% plaster (i.e., $\ll$100 μm) was used in the model (τ_0 $\sim$100 Pa). Models simulate stratocones that have a bulk cohesion of 10^6–10^8 Pa, the approximate cohesion of fresh unfractured rock (Table 1). Test experiments showed that varying cohesion from 25 to 150 Pa, by varying the amount of plaster (from 5 to 40 wt%), did not significantly affect intrusion morphology, except that higher cohesion produced slightly thinner, better-scaled intrusions. The analogue granular mixture has an internal friction angle comparable to that for granular materials at volcanoes (30–40°).

[19] GS, the magma analogue, is a Newtonian fluid simulating dyke propagation in a brittle medium. It approaches the required scaling for viscosity (μ) and time (t) to model basalt to andesite magma propagating in the shallow crust below a volcanic edifice. As it is a Newtonian fluid, time and viscosity ratios can be related to the stress ratio, with equation (2)

$$\sigma^* \approx \frac{1}{t^*} \times \mu^* \qquad (2)$$

where μ^* and t^* are the model/nature ratios for viscosity and time. Combining equations (1) and (2) yields equation (3)

$$\mu_{\mathrm{nature}} = \left(\frac{\mu_{\mathrm{model}}}{t_{\mathrm{model}} \times \rho^* \times g^* \times h^*} \right) \times t_{\mathrm{nature}} \qquad (3)$$

Table 1. List of Parameters Identified as Potential Controlling Factors on Dyke Propagation Under a Volcano Load[a]

Parameter	Definition	Model Reference Value	Nature Reference Value	Model/Nature Ratio	Model Range	Nature Range	Dimension	Source of Data
H_{co}	Cone height	0.05	1000	5×10^{-5}	0.01–0.1	200–4000	L (m)	[1], [2], [3], [4]
R_{co}	Cone radius	0.1	5×10^{3}	2×10^{-5}	0.04–0.13	1×10^{3}–3×10^{4}	L (m)	[3], [5]
$\mathrm{Th_s}$	Substratum thickness	0.1	10^{3}	10^{-4}	0.05–0.2	5×10^{2}–2×10^{3}	L (m)	Following experiment scaling
D_W	Dyke width	2×10^{-3}	1	2×10^{-3}	10^{-3}–10^{-2}	0.25–10 50–100 m for silicic dykes	L (m)	[3], [6], [7], [8], [9], [10]
D_L	Dyke length	0.1	10^{3}	10^{-4}	0.05–0.02	2×10^{2}–>1×10^{3}	L (m)	[3], [8], [9], [10], [11]
Δx	Distance extrusion point-cone summit	0.1	5×10^{3}	2×10^{-5}	0–0.1	0–3×10^{4}	L (m)	Scaling with R_{co}
ρ_{co}	Substratum/Cone density	1425	2400	0.60	1350–1500	2150–2700	$M \cdot L^{-3}$ (kg/m^3)	[1], [3], [4], [12]
τ_0	Substratum/Cone cohesion	100	10^{7}	10^{-5}	100	2×10^{6}–1×10^{7}	$M \cdot L^{-1} \cdot T^{-2}$ (Pa)	[1], [13]
Φ	Internal angle of friction	30–40°	30–40°	1	30–40°	30–40°		
μ	Intrusion dynamic viscosity	70	10^{4}	7.10^{-3}	70	10^{2}–10^{6}	$M \cdot L^{-1} \cdot T^{-1}$ (Pa s)	[3], [14]
ρ_I	Intrusion density	1300	2400	0.55	1200–1400	2300–2700	$M \cdot L^{-3}$ (kg/m^3)	[3], [4], [14]
g	Gravitational acceleration	9.81	9.81	1			$L \cdot T^{-2}$ (m.s^{-2})	
ΔP	Dyke overpressure	5×10^{3}	5×10^{6}	10^{-3}	10^{2}–10^{4}	10^{6}–10^{7}	$M \cdot L^{-1} \cdot T^{-2}$ (Pa)	[3], [4], [15]
f	Intrusion rate	5×10^{-8}	10^{-1}	5×10^{-7}	10^{-8}–10^{-7}	10^{-4}–10^{2}	$L^{3} \cdot T^{-1}$ (m^3 s^{-1})	[3], [4], [15]
T	Time	2×10^{3}	2×10^{5}	10^{-2}	5×10^{2}–1×10^{4}	5×10^{3}–5×10^{7}	T (s)	[3], [15], [16]

[a] Typical range of values for scoria cones to oceanic shields are given and used to estimate key dimensionless parameters in Table 2. References: [1] *Shteynberg and Solovyev* [1976]; [2] *Francis and Oppenheimer* [2003]; [3] *Pinel and Jaupart* [2000]; [4] *Pinel and Jaupart* [2004b]; [5] *Rowland and Garbeil* [2000]; [6] *Walker* [1995]; [7] *Klausen* [2006]; [8] *Valentine and Krogh* [2006]; [9] *Poland et al.* [2008]; [10] *Valentine and Keating* [2007]; [11] *Valentine and Keating* [2007]; [12] *Gaffney and Damjanac* [2006]; [13] *Jaeger and Cook* [1971]; [14] *Spera* [2000]; [15] *Pinel and Jaupart* [2004a]; [16] *Battaglia and Bachèlery* [2003].

Using a 10^{-4} height ratio, 0.55 density ratio, 0.01–1 time ratio and 70 Pa s analogue magma viscosity (GS viscosity, Table 1), equation (3) generates a natural magma viscosity of the order of 10^{6}–10^{8} Pa s. This is higher than the expected viscosity for basalt magmas. Experiments approach the adequate scaling for andesite dykes, or crystal-rich basalt magma, rising under a low-relief volcano (i.e., cone height <1 km). Test experiments were run using GS with 5 wt% water, reducing the viscosity by an order of magnitude (~6–7 Pa s). These experiments were 5–10 times more rapid, thus scaling to similar natural magma viscosity (~10^{6} Pa s). Observations of dyke morphology, propagation, extrusion location and surface deformation were also mechanically similar. The same scaling considerations are valid considering the substratum thickness, suggesting that experiments are representative of shallow processes occurring in the few first kilometers below the volcano base. The substratum in the experiments corresponds to the upper crust for a dyke rising from the mantle, or from a shallow magma reservoir feeding dykes to an overlying volcano.

[20] The system variability is accounted for by 11 dimensionless numbers (Table 2), derived using the Π-Buckingham theorem [*Middleton and Wilcock*, 1994]. Π_1 to Π_5 characterize the system geometry on which the analysis will focus, as this study aims to identify the effect of volcano size, slope and substratum thickness upon dyke propagation. Dimensional analysis shows reasonable matching between model and nature values (Table 2). Densities, cohesion, gravitational acceleration, viscosity and internal friction angle can be taken as constant as long as the same granular material and intrusion fluid are used. Dimensionless numbers for dynamical parameters, i.e., intrusion rate (Π_{10}) and dyke overpressure (Π_{11}), are also consistent from nature to models although models simulate the upper range of natural values. Intrusion rate is varied in experimental conditions by only one order of magnitude in order to test the sensitivity of the system to this dynamic parameter. The ratio of dyke width to dyke length is only approximatively scaled: experimental dykes tend to be one order of magnitude thicker than natural examples because of intrusion thickening at the end of an experiment by interaction with the surrounding granular material.

[21] As the analogue experiments are not closely scaled for low-viscosity mafic dykes caution is required when interpreting observations. As dykes are relatively thick and emplaced rapidly, observed deformation in experiments will be faster, more extensive and of larger scale than expected in large natural volcanoes. The observed deformation is probably representative of that which affects a poorly coherent, ~500-m-high volcanic cone. The general deformation pattern observed in experiments however might still provide valuable insights for a larger set of natural cases. The expectation from scaling considerations is that the thicker experimental intrusions and the resulting surface deformation could be considered equivalent to the intrusion and deformation generated in nature by more than one similar intrusive event. The fact that in nature vent distributions are similar for small to large volcanoes (i.e., the relationship is scale independent) means that correct modeling of small volcanoes should also provide a correct analogue for larger volcanoes.

Table 2. List of Dimensionless Parameters Identified and Used in the Present Study[a]

Dimensionless Number	Definition	Description	Models	Nature
Π_1	H_{co}/R_{co}	Volcano cone aspect ratio	0.2–0.75	0.1–0.6
Π_2	R_{co}/Th_s	Edifice radius/Substratum thickness	0.3–2.5	0.5–10
Π_3	D_W/D_L	Dyke aspect ratio	10^{-1}–10^{-2}	10^{-2}–10^{-4}
Π_4	D_L/R_{co}	Dyke length/cone radius ratio	0.1–1	0.1–1
Π_5	$\Delta x/R_{co}$	Dimensionless extrusion outbreak position	0–1	0–1
Π_6	ρ_i/ρ_{co}	Magma/granular material density contrast	0.8–0.95	0.85–1
Π_7	$\tau_0/(\mathrm{Th}_s \cdot g \cdot \rho_{co})$	Cohesion/stress ratio	5.10^{-2}	2.10^{-1}
Π_8	$T^2 \cdot g/\mathrm{Th}_s$	Dimensionless intrusion duration	10^7–10^9	10^5–10^{10}
Π_9	$(\rho_I \cdot \mathrm{Th}_s \cdot d)/(T \cdot \mu)$	Reynolds number of intruded fluid[b]	10^{-5}	10^{-1}–10^{-5}
Π_{10}	$f \cdot T/\mathrm{Th}_s^3$	Dimensionless intrusion rate	5.10^{-2}–10^{-1}	10^{-6}–10^{-1}
Π_{11}	$\Delta P/(\mathrm{Th}_s \cdot g \cdot \rho_{co})$	Dimensionless dyke overpressure	0.1–5	10^{-1}

[a] See Table 1 for range of values used in ratio estimation.
[b] Where d is the diameter of the intrusion tube for experiments.

3.2. Experimental Setup

[22] Experiments were designed to investigate the 3D vertical propagation of a dyke approaching a conical volcano, within 1–2 km of the cone base. The setup, originally developed at Laboratoire Magmas et Volcans (Clermont-Ferrand [*Mathieu et al.*, 2008]), consisted of a flat, square, wooden board (400 × 400 × 200 mm) containing the granular material with a fissure-shaped outlet at the basal plate center. A GS reservoir was connected with a plastic tube to the outlet (Figure 5a). Varying reservoir height controlled the intrusion rate and overpressure. The cone was made up of the same material as the substratum. This homogeneous medium enables the volcano load effect to be highlighted. Vertical dyke propagation was initiated by vertically placing a thin frozen sheet of GS (i.e., ~2 × 2 cm; 2 mm thick) above the fissure-shaped aperture (i.e., 5 × 16 mm) through the sand-box base. In one set of experiments (C1 to C5, Table 3), an established magma conduit was simulated in the crust by using a square basal aperture (8 × 8 mm) and an initiated vertical magma analogue conduit, 3 mm in diameter, up to the cone base.

[23] Granular layers were ~5, ~10 or ~20 cm thick (Table 3). Cones of varying size (~10, ~17 or ~24 cm diameter) and slope angle (~10°, ~20° or 30°) were placed over the flat crust above the intrusion hole. Surface deformation, eruption timing and location were recorded using vertical photographs acquired at regular time intervals (i.e., 2–5 min). Once the fluid had extruded, the experiment was stopped and the setup was placed into a freezer and left overnight. The frozen intrusion was then manually excavated and photographed. The deformation pattern for each time interval was extracted by automatic identification and frame-by-frame tracking of black sand grains randomly distributed over the model surface (i.e., using PointCatcher, software written by M.R. James). Table 3 details the experimental conditions. Key results from the 78 experiments are described hereafter and illustrated on Figures 6–10.

3.3. Experimental Results

3.3.1. General Intrusions' Morphology

[24] In a typical experiment, GS injection into granular material forms one or several diverging vertical to subhorizontal planar sheets, ~1 cm in thickness. Intrusions have a bulbous surface texture with surface irregularities of the order of a few millimeters, as described by *Mathieu et al.* [2008]. The intrusion lateral and upper edges are characterized by many nascent lobes which record the shear motion during dyke propagation. The upper tip of the dyke is often formed by several diverging or en-echelon lobes. Each intrusive sheet is several cm long (<20 cm), with the length increasing in the first 3–5 cm above the intrusion point. Maximum intrusion length is higher for thicker crusts. As an intrusion approaches the surface, dyke length and thickness decrease, i.e., the erupting magma sheet is then 2–8 cm long and a few mm thick. The length and thickness decrease is related to an increasing intrusion rate as the dyke gets close to the surface and to the reduced time for intrusion thickening induced by wetting of the surrounding granular material.

3.3.2. Extrusion Point Localization

[25] The main objective of these experiments was to study the effect of the load geometry upon extrusion outbreak location. For crust thicknesses in the 5–10 cm range, the orientation of the extrusion relative to the cone summit is controlled by the initiated dyke orientation. More scatter in relative orientation is observed for thicker crust. The extrusion offset point varied widely with changing experimental conditions, from extrusion at the summit ($\Pi_5 = 0$) to outbreak at the base ($\Pi_5 = 1$). Significant lateral deviation of the extrusion point is associated with simple "dyke", "dyke and sill" or "cup-shaped" intrusions (see hereafter). Despite scatter in the data, the relative extrusion offset can be related to the main geometric conditions of the experiments.

[26] Figures 6a–6c illustrate the variation in the outbreak offset (Π_5) for contrasting experimental geometric conditions. Figure 6a shows that the lateral deviation increases for steeper cones. The average offset is also significantly greater for thicker substratum. A key finding is that it is only for thick substratum ($\mathrm{Th}_s > 15$ cm) and steep volcanoes ($\Pi_1 > 0.6$) that dykes can erupt at the cone base. This is confirmed by Figure 6b that shows that low values of Π_2, the cone radius to substratum thickness ratio, lead to a greater extrusion offset, especially for steep cones. Figure 6c shows a similar trend for the effect of Π_4 (dyke length to cone radius ratio). On average, shorter dykes do not reach the cone base, irrespective of the dyke initiation depth. Longer dykes break out at the base only if the dyke was initiated at sufficient depth. The relative intrusion rate (Π_{10}) and the relative overpressure (Π_{11}) also show negative correlations with the outbreak offset. These parameters are strongly correlated with the geometric ratios, especially Π_2, and thus display similar trends.

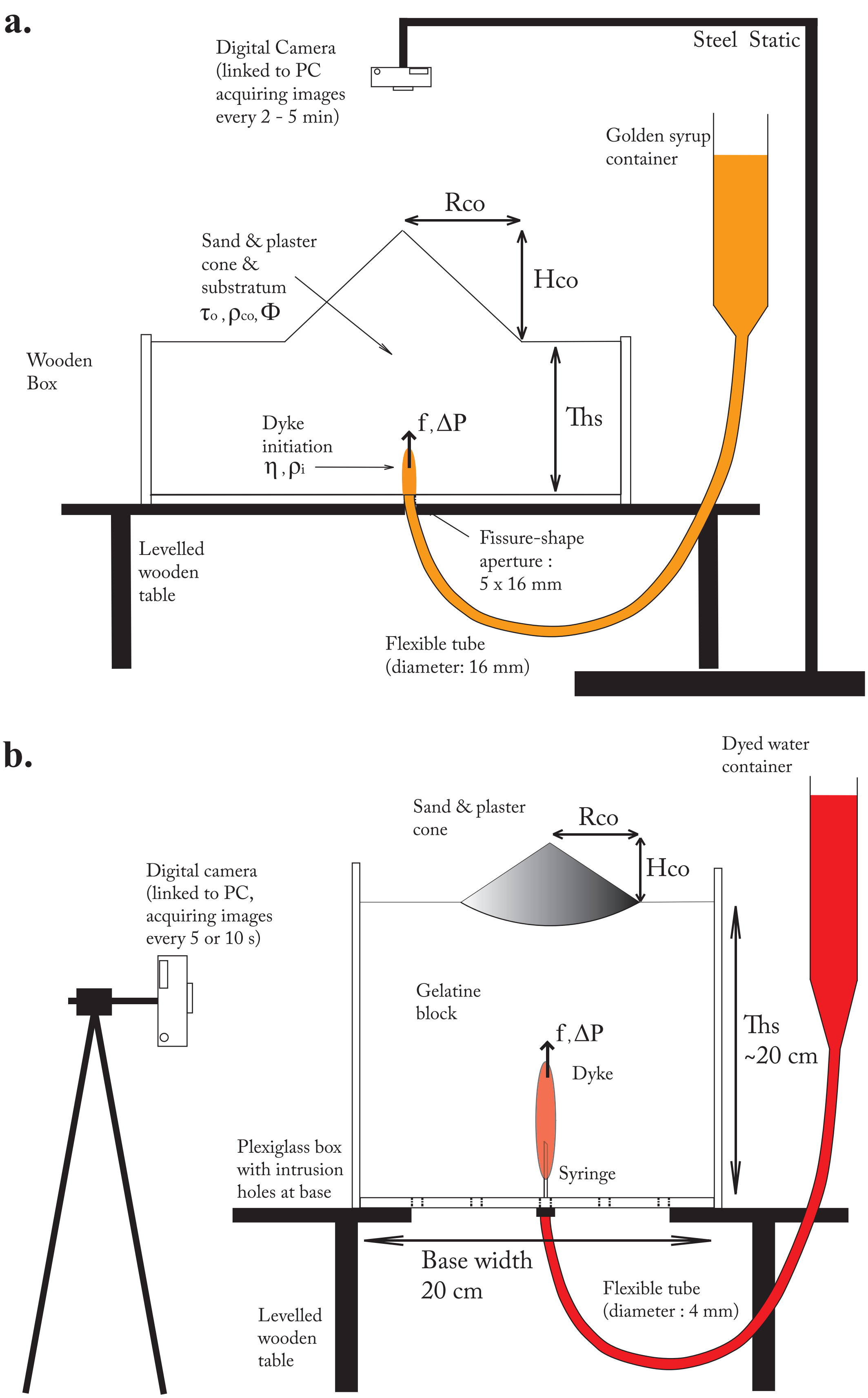

Figure 5. (a) Sketch of the experimental setup of Golden syrup intrusion into a box of fine granular material with indication of main experimental parameters. (b) Sketch of the setup used for injection of dyed water into a tank filled with gelatin.

Table 3. Sand-Box Experiments[a]

Experiment No.	Time (min)	Th_s (cm)	R_{co} (cm)	H_{co} (cm)	Intrusion Rate (cm^3/s)	ΔP (Pa)	Π_1 H_{co}/R_{co}	Π_2 R_{co}/Th_s	Π_3 D_L/D_W	Π_4 D_L/R_{co}	Π_5 $\Delta x/R_{co}$	$\Pi_9 \times 10^{-6}$	Intrusion Shape	Magma Stalling	Lateral Propagation
D31	4	5.0	5.3	3.4	0.09	4940	0.64	1.06	0.10	1.13	0.79	61.9	Dyke and sill complex + chamber	V	V
D32	11	6.4	5.2	3.4	0.07	80	0.65	0.81	0.03	1.06	0.58	28.8	Near-cylindrical conduit		V
D33	34	5.2	5.3	3.8	0.01	1920	0.72	1.01	0.09	1.03	0.67	7.6	Dyke and sill complex	V	V
D34	12	5.2	8.8	5.2	0.04	3930	0.59	1.68	0.02	0.51	0.16	21.5	Deep cup-shaped		
D35	25	5.6	8.4	5.6	0.03	1240	0.67	1.50	0.15	0.62	0.44	11.1	Deep cup-shaped		V
D36	5	5.3	9.3	6.0	0.13	3250	0.65	1.75	0.10	0.32	0.24	52.5	Near-cylindrical conduit		
D37	40	5.4	12.5	8.5	0.06	2490	0.68	2.31	0.20	0.40	0.04	6.7	Dyke and sill complex + chamber	V	
D38	44	5.1	13.2	9.6	0.03	1780	0.73	2.58	0.04	0.52	0.21	5.7	Near-cylindrical conduit		
D41	21	5.3	13.0	9.3	0.14	3260	0.72	2.45	0.08	0.65	0.26	12.5	Dyke and sill complex + chamber	V	
D42	29	5.3	4.8	1.7	0.02	2910	0.36	0.90	0.09	0.95	0.59	9.1	Dyke and sill complex + chamber	V	
D43	4.5	5.0	5.2	1.9	0.13	3900	0.36	1.04	0.44	0.87	0.10	55.0	Near-cylindrical conduit + chamber	V	
D44	22	5.0	8.8	3.5	0.04	1760	0.40	1.75	0.23	0.46	0.03	11.3	Dyke and sill complex	V	
D45	9	5.9	9.0	2.8	0.09	4180	0.31	1.53	0.28	0.28	0.11	32.5	Dyke and sill complex + chamber	V	
D46	35	5.7	13.0	4.9	0.03	2130	0.38	2.28	0.10	0.52	0.38	8.1	Dyke and sill complex	V	V
D47	14	5.0	13.0	4.3	0.08	1830	0.33	2.60	0.07	0.23	0.23	17.7	Dyke and sill complex + chamber	V	V
D48	11	5.0	12.8	4.8	0.11	2790	0.38	2.56	0.15	0.16	0.25	22.5	Deep cup-shaped		
D49	35	5.4	13.1	2.4	0.02	2030	0.18	2.43	0.05	0.31	0.11	7.6	Dyke		
D410	6	5.2	13.2	2.3	0.06	3270	0.17	2.54	0.20	0.15	0.09	42.9	Deep cup-shaped		
D411	81	5.3	12.3	2.3	0.01	2050	0.19	2.33	0.12	0.14	0.03	3.2	Dyke + deep cup-shaped	V	
D412	93	5.3	9.5	1.8	0.01	1930	0.19	1.79	0.50	0.11	0.13	2.8	Near-cylindrical conduit		
D413	16	5.1	8.5	2.0	0.04	2000	0.24	1.67	0.08	0.56	0.33	15.8	Dyke and sill complex	V	V
D414	10	5.4	8.3	1.9	0.07	2970	0.22	1.53	0.10	0.24	0.17	26.7	Deep cup-shaped + chamber	V	
D415	25	10.1	5.6	3.5	0.07	2110	0.62	0.55	0.25	0.50	0.75	20.0	Deep cup-shaped		V
D416	25	10.2	4.8	3.4	0.02	1790	0.71	0.47	0.11	0.38	0.42	20.2	Dyke + near-cylindrical conduit		
D417	46	10.3	4.6	3.2	0.02	1340	0.70	0.45	0.07	0.65	0.52	11.0	Dyke and sill complex + chamber	V	
D51	35	10.1	8.2	5.0	0.06	2250	0.61	0.82	0.09	0.67	0.65	14.2	Deep cup-shaped		V
D52	52	10.1	8.5	5.8	0.03	1640	0.68	0.84	0.04	0.94	0.55	9.6	Dyke and sill complex	V	V
D53	31	10.0	8.4	5.8	0.08	3850	0.69	0.84	0.11	0.44	0.70	16.0	Near-cylindrical conduit + chamber	V	V
H5	60	9.0	9.3	5.0	0.04	2850	0.54	1.03	0.08	0.65	0.54	7.4	Dyke		V
D54	105	10.4	12.4	7.8	0.02	2860	0.63	1.19	0.04	0.45	0.11	4.9	Dyke		
D55	25	10.3	12.4	8.1	0.10	2510	0.65	1.21	0.07	0.36	0.37	20.3	Dyke		V
D56	75	10.1	12.2	7.8	0.02	4140	0.64	1.21	0.05	0.49	0.63	6.7	Dyke and sill complex + chamber	V	V
D57	60	10.2	5.7	2.1	0.02	4690	0.37	0.56	0.15	0.35	0.46	8.4	Dyke and sill complex + chamber	V	
D59	26	10.1	5.1	2.0	0.08	4390	0.38	0.50	0.07	0.53	0.65	19.2	Deep cup-shaped + chamber	V	V
D510	101	10.1	5.3	2.1	0.01	2820	0.40	0.52	0.14	0.42	0.27	5.0	Deep cup-shaped	V	V
D511	19	10.1	8.0	2.8	0.09	3650	0.35	0.80	0.21	0.30	0.48	26.2	Dyke and sill complex	V	V
D512	57	10.1	8.3	3.0	0.02	2670	0.36	0.82	0.13	0.38	0.33	8.8	Deep cup-shaped + chamber	V	V
D513	15	10.2	12.9	4.7	0.13	1450	0.36	1.27	0.47	0.23	0.02	33.5	Near-cylindrical conduit		

Table 3. (continued)

Experiment No.	Time (min)	Th_s (cm)	R_{co} (cm)	H_{co} (cm)	Intrusion Rate (cm^3/s)	ΔP (Pa)	Π_1 H_{co}/R_{co}	Π_2 R_{co}/Th_s	Π_3 D_L/D_W	Π_4 D_L/R_{co}	Π_5 $\Delta x/R_{co}$	$\Pi_9 \times 10^{-6}$	Intrusion Shape	Magma Stalling	Lateral Propagation
D514	59	10.0	12.8	4.8	0.04	1220	0.38	1.28	0.30	0.18	0.50	8.4	Deep cup-shaped	V	V
D515	27	10.3	12.5	4.7	0.07	1550	0.38	1.21	0.11	0.28	0.32	18.9	Near-cylindrical conduit		
D516	28	10.1	8.8	2.0	0.05	860	0.23	0.87	0.22	0.26	0.27	17.9	Dyke		
D517	18	10.2	9.1	2.1	0.07	2380	0.23	0.90	0.60	0.27	0.14	27.9	Near-cylindrical conduit		
D518	100	10.1	9.5	2.1	0.01	1830	0.22	0.94	0.50	0.21	0.25	5.0	Dyke		
D519	40	10.1	12.8	2.5	0.06	2760	0.20	1.27	0.42	0.19	0.38	12.5	Dyke and sill complex	V	V
D520	36	10.0	12.5	2.7	0.03	1860	0.22	1.25	0.02	1.88	0.22	13.8	Dyke and sill complex	V	
D61	17	10.1	12.8	2.7	0.11	2530	0.21	1.26	1.00	0.14	0.12	29.4	Deep cup-shaped	V	
D63	70	19.8	4.9	3.7	0.05	4120	0.76	0.25	0.09	0.71	0.92	14.0	Dyke		V
D64	47	19.8	5.1	3.7	0.09	4550	0.73	0.26	0.13	0.78	1.04	20.9	Deep cup-shaped		V
CL18	103	19.0	6.5	4.6	0.04	9090	0.71	0.34	0.03	2.31	0.89	9.1	Dyke and sill complex		V
D14	100	20.0	6.0	4.5	0.07	9210	0.75	0.30	0.10	0.50	1.17	9.9	Dyke + cup-shaped		V
D66	41	19.8	8.8	5.8	0.09	4340	0.66	0.44	0.08	0.45	0.82	23.9	Dyke		V
D67	67	19.8	8.4	5.2	0.08	2510	0.62	0.42	0.27	0.54	0.93	14.6	Dyke		V
D69	146	19.8	8.9	5.8	0.02	3220	0.65	0.45	0.22	0.51	0.65	6.7	Dyke		V
CL16	55	17.2	9.0	6.9	0.08	11200	0.77	0.52	0.13	0.44	0.67	15.5	Dyke		V
CL21	75	18.0	8.5	6.6	0.05	8320	0.78	0.47	0.09	0.82	0.98	11.9	Dyke		V
D68	74	19.7	12.3	8.9	0.06	2710	0.73	0.62	0.08	0.98	0.69	13.2	Dyke		V
D610	78	19.7	12.2	8.2	0.05	1830	0.67	0.62	0.18	0.45	0.71	12.5	Dyke		V
D611	47	19.8	12.3	8.7	0.13	1710	0.71	0.62	0.07	0.24	0.75	20.9	Dyke		V
D21	150	20.0	10.0	7.0	0.08	9340	0.70	0.50	0.33	0.30	1.20	6.6	Deep cup-shaped		V
CL210	170	21.3	18.0	9.5	0.05	8600	0.53	0.85	0.05	0.33	0.92	6.2	Dyke		V
CL22	87	19.5	12.3	9.8	0.05	8320	0.80	0.63	0.03	1.06	0.90	11.1	Deep cup-shaped		V
D612	59	19.8	8.5	3.9	0.07	3270	0.46	0.43	0.14	0.82	0.89	16.6	Dyke		V
D613	87	19.8	8.4	3.3	0.03	3190	0.39	0.42	0.08	0.60	0.68	11.3	Dyke		
D71	36	19.8	8.7	3.3	0.12	2970	0.38	0.44	0.12	0.57	0.74	27.2	Dyke and sill complex	V	V
D72	156	19.8	11.7	5.1	0.04	2730	0.44	0.59	0.26	0.46	0.79	6.3	Dyke		
D73	56	19.8	12.7	4.7	0.09	6490	0.37	0.64	0.05	0.47	0.25	17.5	Dyke and sill complex	V	
D75	65	19.8	12.7	4.5	0.07	2990	0.35	0.64	0.04	0.41	0.76	15.1	Dyke		V
D76	60	19.8	9.5	2.0	0.07	3490	0.21	0.48	0.20	0.26	0.57	16.3	Dyke	V	
D77	121	19.8	9.2	2.1	0.02	3930	0.23	0.46	0.09	0.49	0.68	8.1	Dyke		V
D78	44	19.8	9.4	1.8	0.11	3610	0.19	0.47	0.12	0.64	0.41	22.3	Dyke		
D81	59	19.8	12.0	2.6	0.05	4010	0.22	0.61	0.12	0.35	0.20	16.6	Dyke		
D82	61	19.8	12.8	2.4	0.05	2330	0.19	0.64	0.08	0.59	0.78	16.1	Dyke		V
D83	39	19.8	12.3	2.4	0.13	2590	0.20	0.62	0.03	0.53	0.78	25.1	Dyke and sill complex	V	V
C1*	18	10.1	12.0	8.8	0.08	860	0.73	1.19	0.20	0.13	0.13	27.8	Near-cylindrical conduit + chamber	V	
C2*	12	11.1	8.5	6.5	0.03	1510	0.76	0.77	0.08	0.47	0.35	45.8	Near-cylindrical conduit		V
C3*	17	10.3	5.7	3.8	0.03	200	0.67	0.55	0.20	0.26	0.44	30.0	Near-cylindrical conduit		V
C4*	44	10.1	12.5	8.7	0.03	920	0.70	1.24	0.15	0.16	0.38	11.4	Near-cylindrical conduit	V	V
C5*	28	10.2	11.8	4.5	0.02	2000	0.38	1.15	0.50	0.09	0.09	18.0	Near-cylindrical conduit	V	

[a] Summary of run conditions and key observations, including relative distance of eruption outbreak (Π_5) and main intrusion shape. For all experiments, a vertical dyke was initiated, except for those experiments marked by an asterisk, where a pre-established conduit was modeled up to the cone base with Golden syrup. Intrusion rate and dyke overpressure (ΔP) are affected by errors of ~5%. Evidence for magma stalling or for lateral propagation is based on the intrusion morphology and on the Π_5 value.

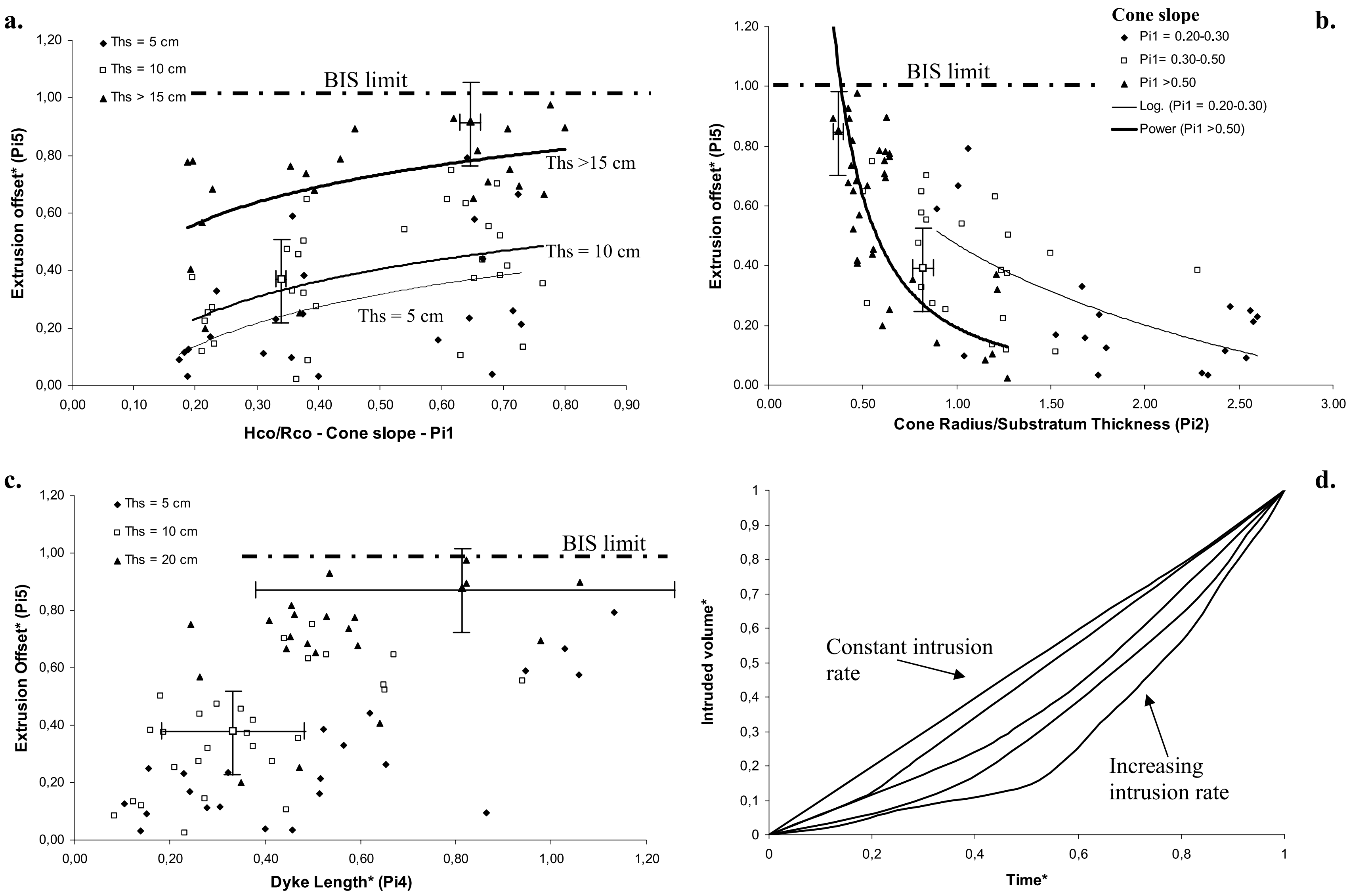
a.
Ths = 5 cm
Ths = 10 cm
Ths > 15 cm
BIS limit
Ths >15 cm
Ths = 10 cm
Ths = 5 cm
Extrusion offset* (Pi5)
1,20
1,00
0,80
0,60
0,40
0,20
0,00
0,00
0,10
0,20
0,30
0,40
0,50
0,60
0,70
0,80
0,90
Hco/Rco - Cone slope - Pi1
b.
Cone slope
Pi1 = 0.20-0.30
Pi1= 0.30-0.50
Pi1 >0.50
Log. (Pi1 = 0.20-0.30)
Power (Pi1 >0.50)
BIS limit
Extrusion offset* (Pi5)
1.20
1.00
0.80
0.60
0.40
0.20
0.00
0.00
0.50
1.00
1.50
2.00
2.50
3.00
Cone Radius/Substratum Thickness (Pi2)
c.
Ths = 5 cm
Ths = 10 cm
Ths = 20 cm
BIS limit
Extrusion Offset* (Pi5)
1,20
1,00
0,80
0,60
0,40
0,20
0,00
0,00
0,20
0,40
0,60
0,80
1,00
1,20
Dyke Length* (Pi4)
d.
Constant intrusion rate
Increasing intrusion rate
Intruded volume*
1
0,9
0,8
0,7
0,6
0,5
0,4
0,3
0,2
0,1
0
0
0,2
0,4
0,6
0,8
1
Time*

Figure 6

[27] Using multivariate linear regression, the influence of the different input parameters upon the relative extrusion offset Π_5 can be quantitatively assessed. 80% of the variability in Π_5 (i.e., estimated from adjusted R^2) is accounted for by a linear regression of the experimental dimensionless ratio parameters. The best-fit model is expressed by the equation

$$\Pi_5 = 1.19\,\Pi_1 - 0.114\,\Pi_2 \quad \left(\text{adjusted } R^2 = 0.81\right) \tag{4}$$

This model confirms that the extrusion offset is greater for steeper cone. The relative depth of initiation appears as the second most important factor. Considering other experimental parameters does not significantly improve the fit of these models.

[28] A main limitation of the experiments is that there is inherent randomness in the experimental system caused by sensitivity of runs to small changes in initial conditions. This includes local heterogeneity in the sand-plaster mix or nonuniform compaction of the material. In order to evaluate how much scatter can be attributed to random variations in experimental conditions, two representative experiments were repeated six times (e.g., experiments D511 and D67). Results (i.e., error bars in Figures 6a–6c) show that Π_5 varies by ±15% for one set of initial conditions but that the average results for the two contrasting sets of conditions are significantly different from each other. Dynamic parameters such as time, intrusion rate and dyke overpressure are affected by variations of up to ±20%. The greatest variation in the observed results for one set of experimental conditions was recorded for the dyke length (i.e., ± 50%, Figure 6c). This is to be related to the significant variation in the morphology of the upper part of the intrusion observed when repeating the same experiment.

3.3.3. Intrusion Rate

[29] The mean intrusion rate imposed by the GS reservoir head ranged from 10^{-8} to 2.10^{-7} m^3 s^{-1} (i.e., 30–450 cm^3 h^{-1}). Despite the near-constant driving overpressure for the intruded fluid throughout the experiment, i.e., the liquid level in the container did not vary much (<10% of ΔH), the injection rate varied significantly throughout the course of a given experiment. At the start, the intrusion rate tended to be low. For some failed experiments, the liquid overpressure was not sufficient to enable dyke propagation. For other experiments intrusion rate was constant, but in most cases the intrusion rate increased, by as much as a factor of ten, when the dyke approached the surface (Figure 6d), as documented in gelatin models by *Rivalta and Dahm* [2006] (see also the work of *Kavanagh et al.* [2006] and *Menand* [2008]). The increasing intrusion rate in injection experiments at constant pressure is consistent with observations of a hyperbolic decrease in overpressure as the fracture develops in injection experiments at constant flow rate [*Murdoch*, 1993a, 1993b, 1993c; *Galland et al.*, 2007]. This behavior results from the fact that larger fractures are weaker than smaller ones. We did not record any experiments in which the intrusion rate decreased when the intrusion approached the cone base.

3.3.4. Variations in Intrusion Morphology, Deformation and Cone Load

[30] Significant contrasts in the morphology of intrusions and in the surface deformation patterns were observed for varying experimental conditions (Figures 7–10). Although the focus is on the location of outbreaks, these other aspects of the experiments are briefly described hereafter as they provide insights into the effect of cone load upon intrusion propagation and as they enable to relate experimental observations to numerical models and natural cases.

[31] Cone load significantly affects dyke propagation within 2–10 cm of cone base depending on crust thickness, causing intrusions to develop horizontally into reservoirs, sills or asymmetric dykes. Deformation structures develop mostly in the second half of an experiment, as the dyke approaches the cone base or intrudes the cone itself. Propagation of subhorizontal intrusions is associated with the most intense deformation, especially when the cone is steep. In the following paragraphs, the end-member intrusion morphologies and associated surface deformation patterns are described. Most intrusions present characteristics of several of these end-members. The experimental conditions cannot be straight forwardly related to a single type of intrusion shape, suggesting that intrusion morphology can vary within some range for the same experimental conditions because of its sensitivity to small changes in initial conditions.

3.3.4.1. Cylindrical Conduit

[32] As illustrated for experiment D53 on Figure 7, some intrusions present a near-cylindrical conduit-like geometry. These intrusions are often associated with a level of symmetrical horizontal propagation, resembling an irregular-shaped ellipsoidal reservoir. These types of structures are most common in experiments with relatively thin crust ($\Pi_2 > 1$) and for steep cones ($\Pi_1 > 0.4$). Surface deformation is significant, with bulging on one flank and asymmetric extension along normal faults at the summit (Figures 7 and 10d), especially when associated with the inflation of a reservoir-like structure. These intrusions are associated with limited deviation of the intrusion from the cone axis (Figure 10d). Conduit-like geometry is characteristic for intrusions developing mostly or directly into a cone at high intrusion rate [*Dumaisnil*, 2007].

3.3.4.2. Vertical Dyke

Figure 6. Results of GS injection in granular media: (a) relative deviation of extrusion point (Π_5) against the cone slope (Π_1); (b) relative deviation of extrusion point (Π_5) against the ratio of cone size to substrate thickness (Π_2); (c) relative deviation of extrusion point (Π_5) against the dyke length relative to the cone radius (Π_4). Trend lines indicate general trend of outbreak offset for a specific set of parameters. These lines are best-fit lines using a logarithmic law in Figure 6a, and a power-law or logarithmic law in Figure 6b as indicated. Error bars indicate one standard deviation of results for two experiments repeated six times with the same input parameters. Variability on relative dyke length is too large to highlight a significant trend. Longer dykes are obtained for thicker crust. (d) Dimensionless volume versus dimensionless time for five representative experiments, showing progressive increase in intrusion rate.

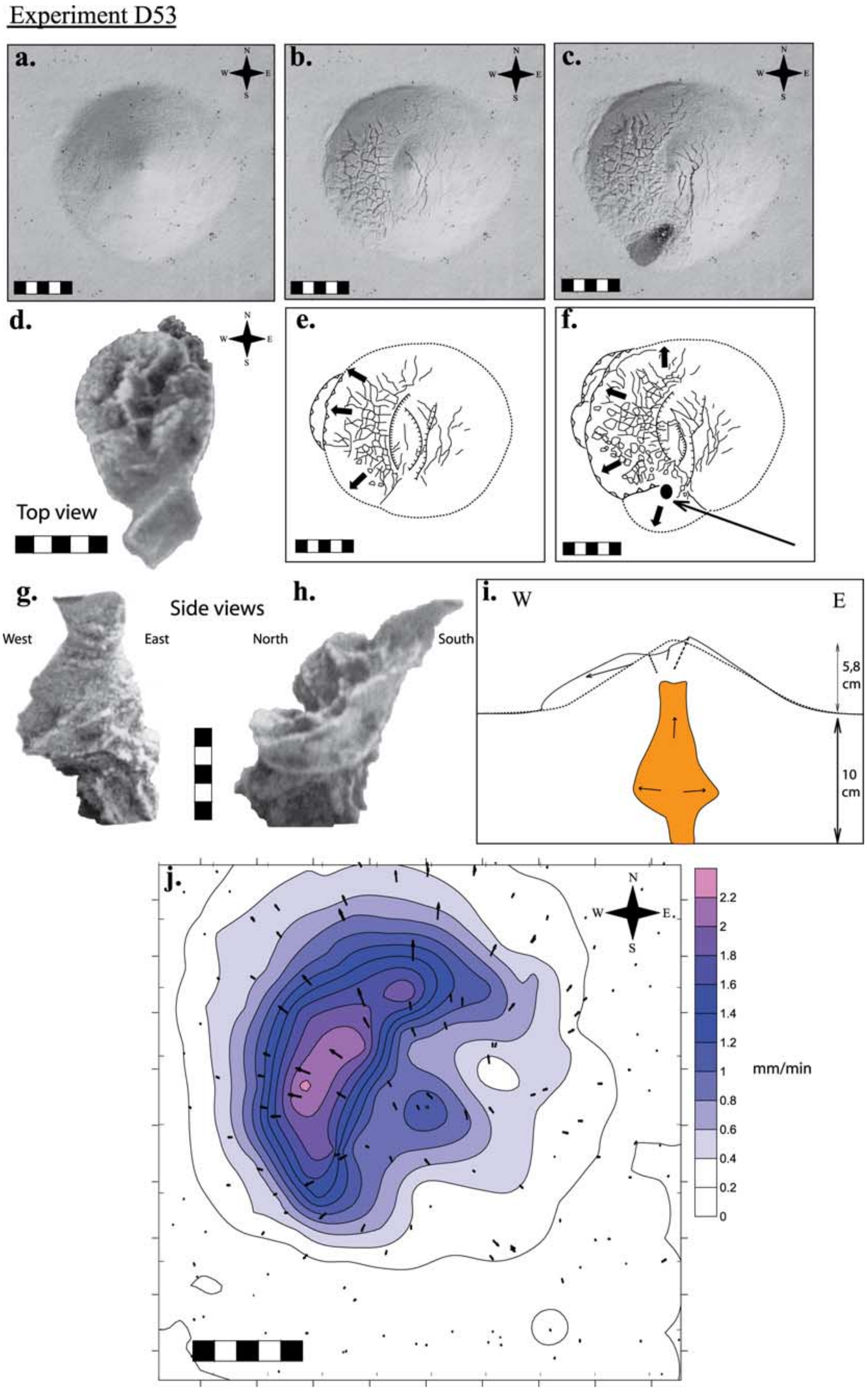
Experiment D53
a.
b.
c.
N
W
E
S
d.
Top view
e.
f.
g.
Side views
West
East
North
South
h.
i.
W
E
5,8 cm
10 cm
j.
2.2
2
1.8
1.6
1.4
1.2
1
0.8
0.6
0.4
0.2
0
mm/min

Figure 7

[33] Figure 8a illustrates the simplest case, where a vertical dyke ascends to within 2 cm of the cone base. The dyke is characterized by an asymmetric upper tip: below the cone summit, the intrusion reaches a lower elevation than its outermost extension; the latter breaches the surface on the lower cone flank (Figure 10b). In some experiments, both lateral extensions of the dyke are able to rise higher than the central part, reflecting the compressive stress gradient below the cone. Dyke intrusion is observed for thick crust ($\Pi_2 < 1$) and low relative dyke overpressure (Median $\Pi_{11} = 1.3$). Dyke asymmetry and extrusion deviation from the cone's central axis are both most pronounced for steeper cones ($\Pi_1 > 0.4$). Surface structures are of limited extent for low-angle cones, with a graben structure forming at the dyke apex. For steep cones, summit extension steepens the lower flanks, causing local collapses.

3.3.4.3. Cup Shape

[34] The upper part of the intrusion can have an elongated cup shape (Figure 8b). This cup originates from a dyke. The observed intrusion shape is consistent with cup intrusion into oblique conjugate faults forming at the dyke tip, as described by *Mathieu et al.* [2008]. In most cases, the cup is elongated in plan view in the same direction as the feeder dyke and develops obliquely in one direction (seen in cross section, Figure 8b). This intrusion type causes general inflation and significant fracturing of the entire cone. Summit subsidence is observed when extrusion is significantly offset from the summit ($\Pi_5 > 0.4$). This intrusion type is intermediate between "conduit-shape/reservoir" intrusions and "dyke and sill" complex and forms for $\Pi_2 \approx 1$.

3.3.4.4. "Dyke and Sill" Complex

[35] In other cases (Table 3) intrusions form a "dyke and sill" complex, with a subvertical and a subhorizontal part (Figures 9 and 10c). The subhorizontal part develops as a sill intrusion, enhancing lateral surface deformation. The dyke part is typically curved, concave toward the sill. Extrusion generally occurs at one extremity of the ellipse formed by the dyke and sill seen in plan view. Deformation starts with the outward migration of the lower portion of the flank situated above the sill. As the flank bulges outward, it causes slope oversteepening and small-scale avalanches. Linear to horseshoe-shaped normal faults accommodate for extension of the bulging flank, bordering it. These normal faults are accompanied by downward-propagating radial fractures in the bulging flank. A second set of normal faults, antithetic to the first opened faults, appears on the opposite flank causing summit subsidence and formation of a crescent-shaped asymmetric summit graben (Figure 9). The dyke propagates within the second set of normal faults bordering the graben structure. The final pattern of the main cracks closely reflects the orientation of the shallowest intrusive sheets (Figure 9). Formation of circular and shallow thrust faults at the cone base is also sometimes observed in association with emplacement of subhorizontal intrusive sheets under the bulging flank.

3.3.4.5. Pre-Established Cylindrical conduit

[36] When a cylindrical conduit reaching the cone base was made before the experiment, the intrusion always followed the established conduit, causing it to inflate to reach 2–3 cm in diameter (Figure 10e). At the conduit top, the magma analogue forms one or two conjugate inclined sheets within the cone. Extrusion takes place close to the cone summit. Surface deformation is characterized by bulging of one cone flank and asymmetric subsidence, bordered by faults cutting through the summit.

4. Dyke Propagation in Gelatin

4.1. Analogue Material

[37] Gelatin is a transparent, brittle, viscoelastic solid with low rigidity and Poisson ratio of ~0.5. Prior to stress disturbance (e.g., loading), the stress condition in gelatin is nearly hydrostatic [*Watanabe et al.*, 2002]. The scaling of gelatin models is difficult because the fracture resistance of a crack tip is large [*Takada*, 1990]. In the natural case, fracture resistance is not the dominant resisting force upon dyke ascent; magma viscous drag dominates the resisting force. Gelatin is an isotropic and homogeneous medium, whereas rocks contain numerous cracks. Despite these limitations, crack propagation observed in stressed gelatin provides relevant insights for tensile crack propagation in the lithosphere. As gelatin models are not adequately scaled to nature, the models presented hereafter are used to further visualize the effect of volcano load upon dyke ascent but not to derive quantitative results.

4.2. Experimental Setup and Methodology

[38] Experiments were conducted in a plexiglass container (0.3 × 0.2 × 0.3 m) with equally spaced injection points along two perpendicular lines at its base (Figure 5b). Pigskin gelatin, with 250 Bloom grade number, diluted in water to a concentration of 3 wt% was used. On the basis of gelatin characterization in previous studies, it is expected that the gelatin has a density of 1008 ± 2 kg m^{-3} [*Watanabe et al.*, 2002], Young's modulus of $\sim 2-5.10^3$ Pa [*Kavanagh et al.*, 2006] and shear modulus of $\sim 5.10^2$ Pa [*Muller et al.*, 2001; *Rivalta and Dahm*, 2006]. The gelatin solution is prepared at 80°C and kept at this temperature until all dissolved. It is then placed in a fridge at 4°C overnight. A thin silicon oil layer is poured on top of the solution to inhibit water evaporation during the cooling process.

[39] Using a similar setup as that used for GS injection into granular material (Figure 5b), dyed water was injected at constant overpressure through a syringe needle at the base

Figure 7. Illustration of experiment D53 results showing the formation of a chamber joined to the surface by an oblique intrusion, associated with the formation of a summit graben and major flank bulging. (a–c) Top views of initial, intermediate, and final model surfaces, and (e–f) interpretation of the deformation structures (arrow pointing to extrusion point); (d) top and (g, h) side views of the excavated intrusion; (i) sketch of a cross section through the model showing the relationship between intrusion and cone deformation; (j) early deformation field (i.e., halfway through the experiment when control points can still be recognized between successive images). Colour scale and contours (0.2-mm/min interval) show horizontal displacement velocity with vectors giving the orientation of surface displacements (derived using PointCatcher, software written by M. R. James). Scales are 5 cm long.

a. Experiment D612

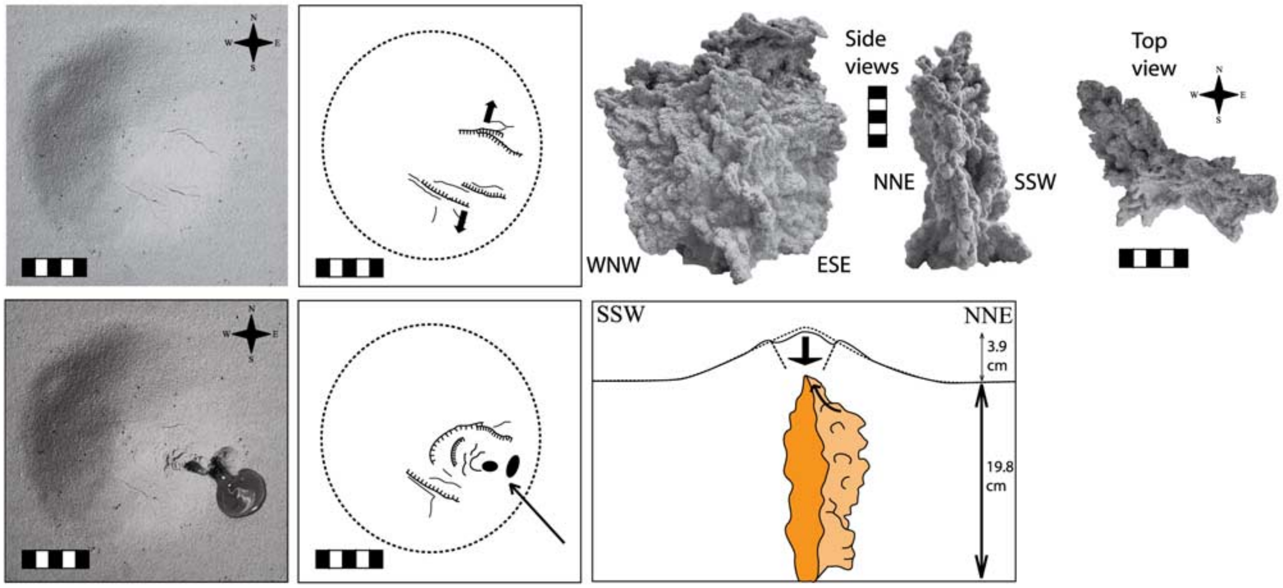

b. Experiment D514

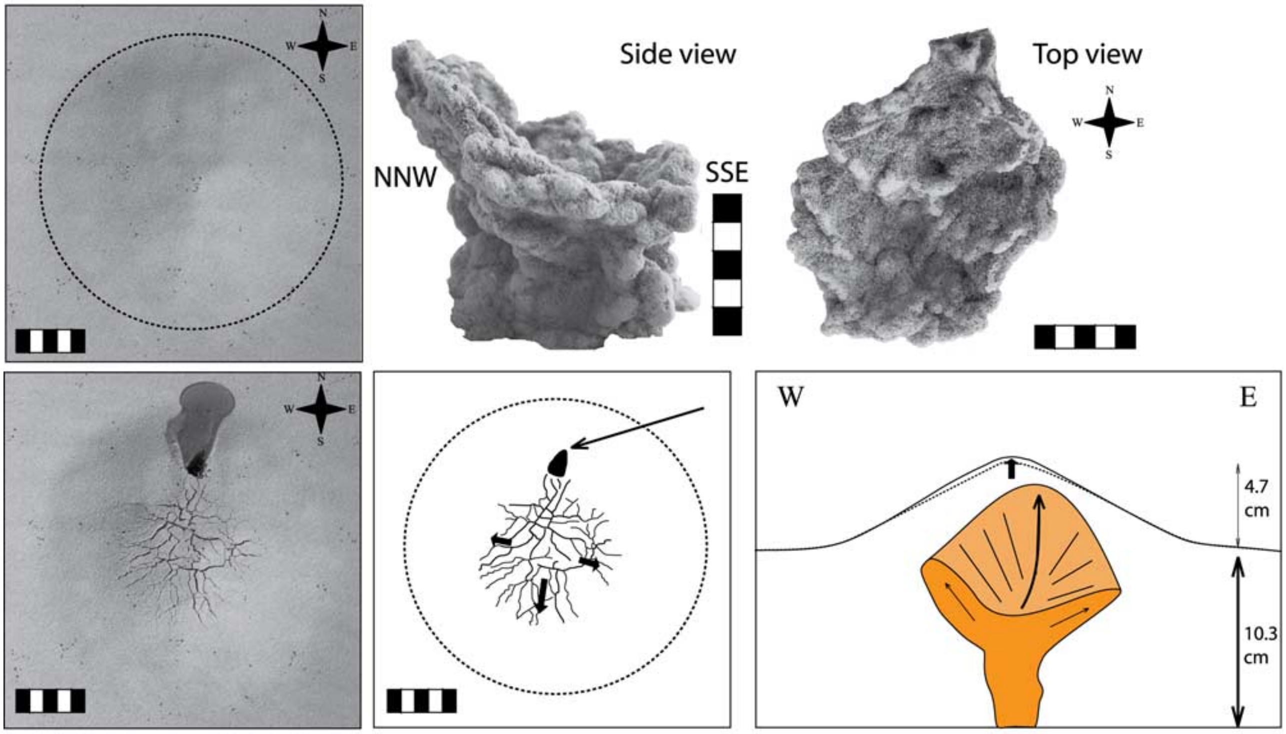

Figure 8. Illustration of (a) experiment D612 and (b) experiment D514. (a) D612 shows a typical dyke with an asymmetric height profile. The dyke outbreaks close to the cone base. Dyke ascent is associated with a minor extension above the dyke tip, focusing close to the outbreak location at the end of the experiment. (b) D514 shows an asymmetric cup-shaped intrusion above a dyke developing away from the cone summit. Intrusion is associated with summit fracturing and bulging.

of the gelatin block. Dyke orientation was controlled by cutting an initial fissure into the gelatin base with a syringe tip. As the density contrast between injected water and gelatin is low, the intrusion is mostly driven by liquid overpressure rather than by buoyancy. To simulate buoyancy-driven dyke ascent, 2 ml of air was manually injected in other experiments and left to rise under buoyancy. Volcano load is simulated using a cone made up of granular material. Using a deformable load, rather than a metal bar as done by *Muller et al.* [2001] or *Watanabe et al.* [2002],

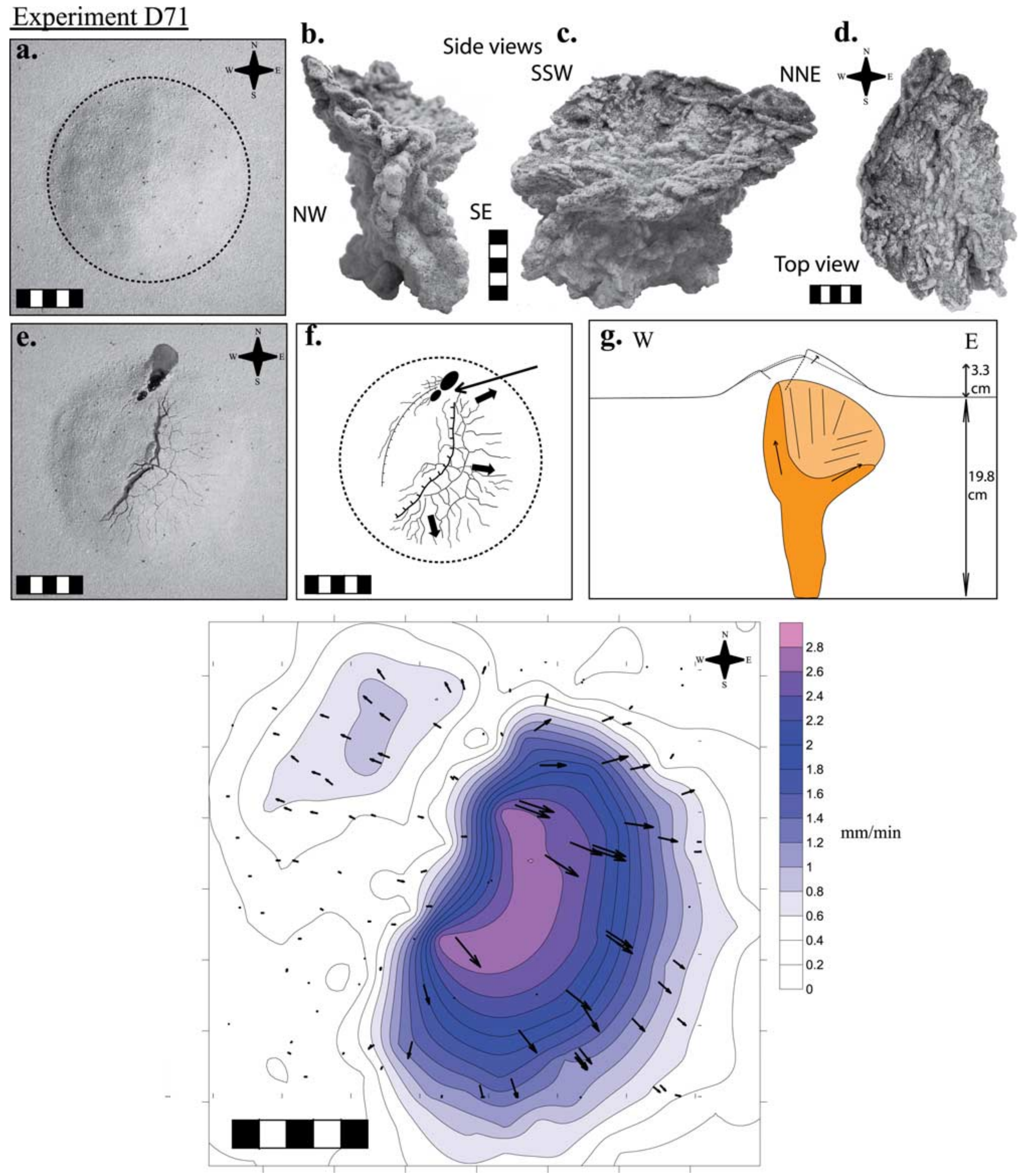

Figure 9. Illustration of experiment D71 showing a dyke and sill complex intrusion associated with an asymmetric graben. (a, e) Top views of initial and final model surfaces and (f) interpretation of the deformation structures (arrow pointing to extrusion point); (b–c) side and (d) top views of the excavated intrusion; (g) sketch of a cross section through the model showing the relationship between intrusion and cone deformation; (h) deformation field during the time elapsed between 6 and 3 min prior to extrusion. Colour scale and contours (0.2-mm/min interval) show horizontal displacement velocity with vectors giving the orientation of surface displacements (derived using PointCatcher, software written by M. R. James). Scales are 5 cm long.

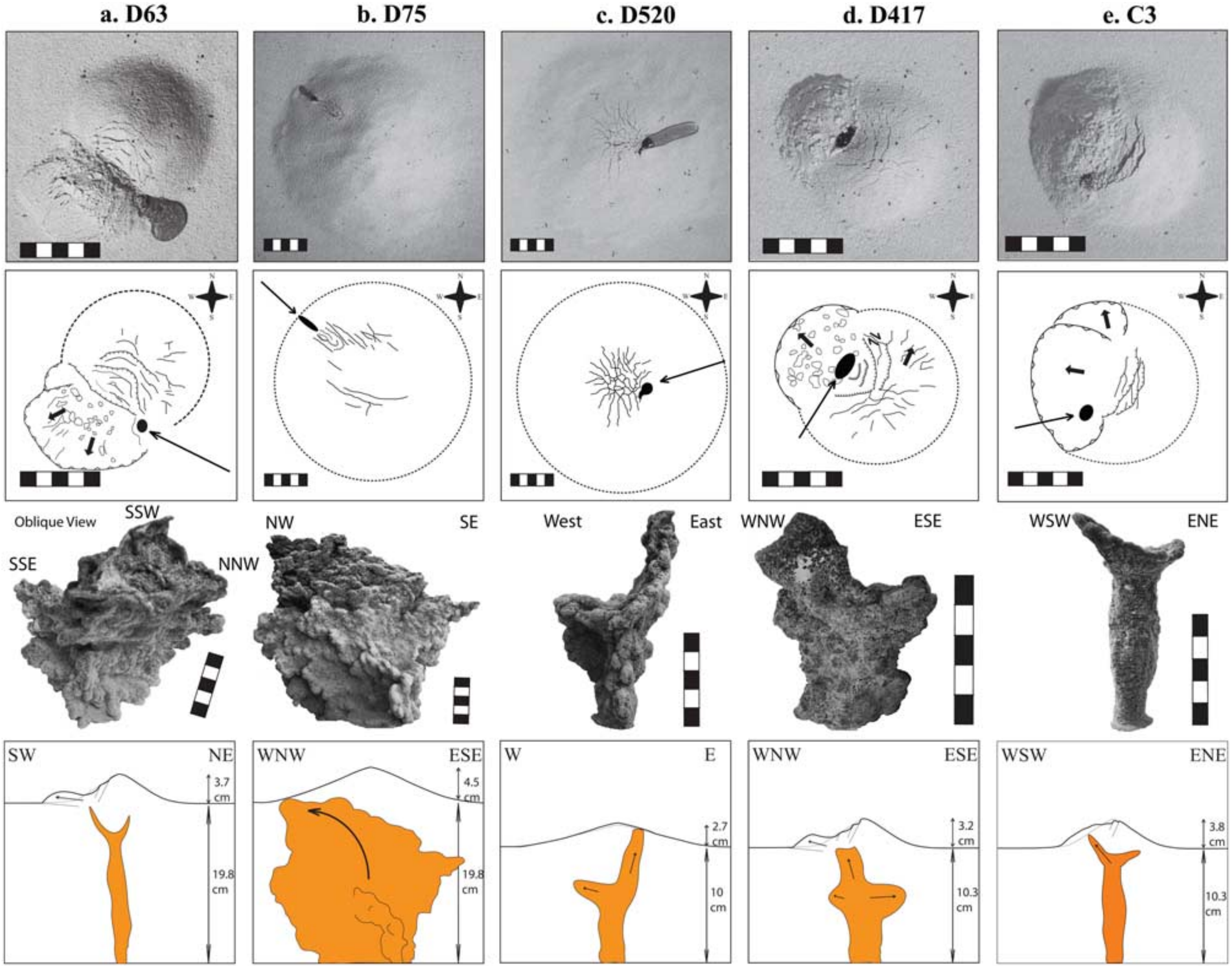

Figure 10. Illustration of contrasted types of experiments: (a) D63: asymmetric dyke dividing into two complementary oblique sheets close to the surface; (b) D75: asymmetric dyke with a minor dyke branch perpendicular to the main one in the lower part. Outbreak occurs at BIS and is associated with minor deformation due to low slope angle; (c) D520: dyke and sill complex below a broad, but low-slope-angle cone, associated with minor deformation; outbreak is close to summit; (d) D417: chamber growth below a narrow steep cone with outbreak of a thick oblique sheet and major flank deformation; (e) C3: near-cylindrical conduit-shaped intrusion formed after the initiation of a narrow conduit up to cone base; within the cone, the intrusion turns into a subhorizontal intrusion sheet.

enabled us to reproduce the 3D reorientation of stresses below a conical edifice. The higher density of the cone relative to the gelatin results in an enhanced effect of the load on the stress field in the gelatin. Dyke propagation was visualized by taking photos from the side at regular time intervals (Figure 11). Ten experiments were carried out under similar conditions and cone load. For three of them air was injected instead of dyed water.

4.3. Experimental Results

[40] For dykes offset from the cone axis and initiated in a direction perpendicular to that defined by the cone summit-injection point line, the dyke propagates toward the cone symmetry axis as described in previous studies [*Muller et al.*, 2001; *Watanabe et al.*, 2002]. When injected below the cone apex, dykes rose vertically.

[41] The key observation in all experiments is the stalling of the rising dyke when approaching the cone base. A marked decrease in upward propagation velocity occurred ~5–8 cm below the cone base (depth ~1–1.5 cone radius, Figure 11). If water injection is stopped at this point, the dyke does not reach the surface. When injection is continued, the dyke continues rising vertically at very low velocity and significantly enlarges horizontally. The dyke develops two lateral lobes, one often being favored. The dyke breaches the surface once one lobe reaches the cone base (Figure 11a). It is not the outermost part of the dyke that breaches the surface. If the initial intrusion point is offset from the cone apex along the dyke propagation plane, the dyke propagates asymmetrically toward the nearest point of the cone base. Extrusion fissures initiate within a centimeter from cone base. They are ~2 cm long, with a radial or subradial orientation relative to the cone summit.

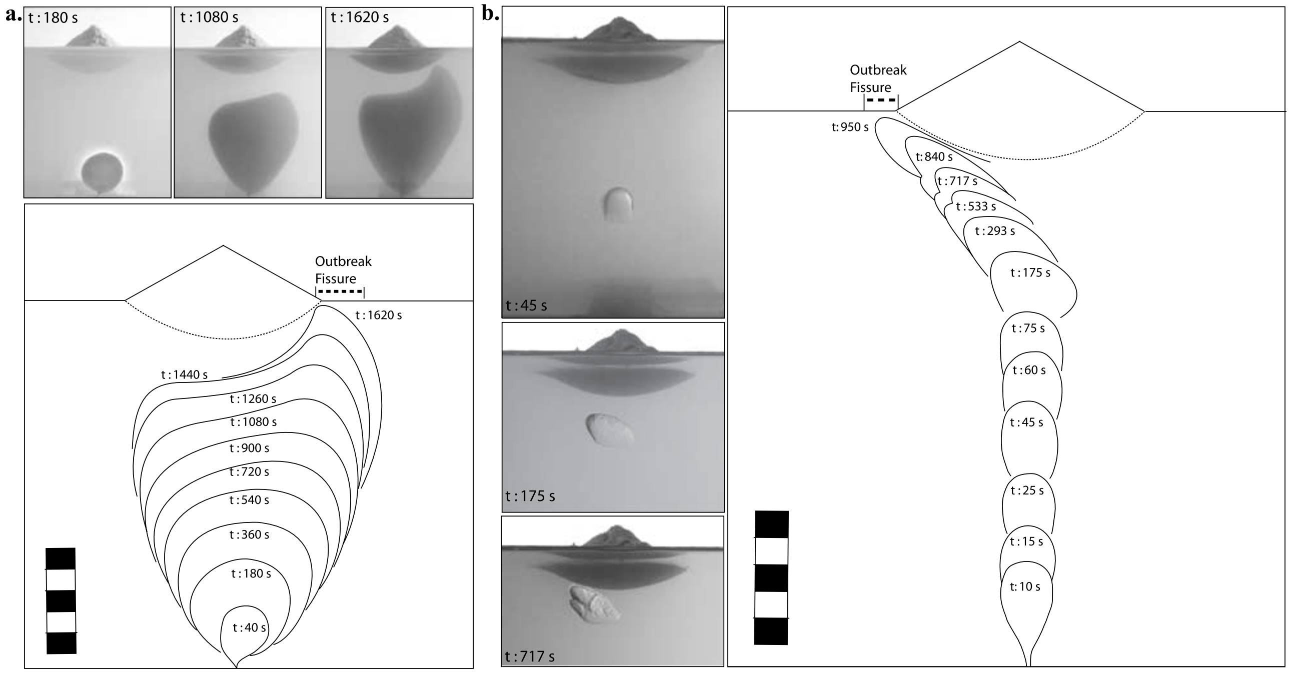

Figure 11. Illustrations of observations from (a) dyed water and (b) air injections into a gelatin block overlain by a sand and plaster cone. Lines show the outline of the intrusion at different time steps. Photos illustrate the intrusion shape at specific time *t*. Evolution of the dyke outline for both types of experiments illustrates that the dyke rise velocity decreases when approaching the cone base. The dyke propagates laterally until extrusion is possible at the cone base. Air injection due to its lower density, forms a small dyke which rises buoyantly and is able to approach closer to the cone base interface. Scales are 5 cm long.

[42] Some dykes, which stalled below the cone base without expanding laterally because of lack of additional fluid injection, were observed to rise and erupt directly after the cone load was removed from the gelatin surface. This illustrates that it was the volcano load that prevented dykes from reaching the surface. It suggests that unloading processes (i.e., flank collapse, caldera formation or erosion) can trigger eruption of magma stored in the central part of the system, as proposed by *Pinel and Jaupart* [2000].

[43] When air is injected, the dyke starts stalling at ~4 cm from the cone base (depth ~ 0.8 cone radius). This great decrease in dyke vertical velocity is associated with a drastic decrease in the dyke aspect ratio (dyke height/length), the dyke length being greater than its height close to the extrusion point (Figure 11b). Air dykes reached within a few millimeters of the cone-gelatin interface but were not able to break through the gelatin surface. Air dykes propagate laterally at a low rate until being able to breach the surface at the cone base. The fact that air dykes can approach closer to the cone-gelatin interface than water dykes before being affected by the cone load suggests that stalling and lateral propagation effects depend on the balance between dyke buoyancy and edifice-induced stress.

5. Discussion

5.1. Volcano Load Effect on Dyke Propagation

[44] Both types of experiments provide insights into the effect of edifice load upon dyke propagation and extrusion point location. In both cases, cone load inhibits vertical dyke ascent and promotes lateral intrusion propagation. For most experiments simulating dyke ascent underneath a steep stratovolcano without opened conduit, extrusions occurred at the base or within the lower flanks, except for thin substratum. In the latter case, the dyke could not develop a sufficient length to reach cone base and the dyke developed within the cone.

[45] Gelatin models allow observation of the propagation and evolution of planar dyke sheets with a simple geometry. They do not render the complexity of intrusions observed in nature. This is due to the fact that gelatin is too stiff and cannot break under shear, as rocks do. Sand-box models are more suitable analogues and result in complex intrusion morphologies, consistent with field observations [e.g., *Emeleus and Bell*, 2005; *Mathieu et al.*, 2008]. Intrusions with multiple branches associated with important changes in propagation direction, sills or oblique intrusions were observed to form.

[46] Analogue experiments allow identification of the main controlling parameters on the dyke propagation system beneath a volcano. For sand-box experiments, cone aspect ratio (Π_1), cone height and relative crustal thickness (Π_2) are the fundamental parameters controlling the offset of the extrusion outbreak (Π_5). Although the effect of each parameter was not constrained for the gelatin models, it is expected that the lateral deviation of the intrusion will increase with cone height or cone slope and decrease with increasing dyke overpressure or density contrast.

[47] The increasing load can ultimately prevent vertical magma ascent in the edifice axial zone, the threshold

depending on the magma density and overpressure [*Carr*, 1984; *van Wyk de Vries and Borgia*, 1996; *Pinel and Jaupart*, 2000]. If a dyke cannot erupt through the volcano axial zone, magma either is intruded beneath the edifice and stored in the axial zone, as observed in our gelatin models with limited intrusion volume, or propagates laterally to feed a distal flank eruption [*Pinel and Jaupart*, 2004a, Figure 12a]. A key control upon dyke ascent or storage is the relative magnitude of the dyke driving pressure and edifice-induced stress.

[48] To compare our experimental results with numerical predictions of *Pinel and Jaupart* [2000, 2004b], GS intrusions were classified on the basis of the evidence for intrusion stalling and/or lateral propagation. Intrusion stalling was characterized by a reservoir-like feature or a level of greater horizontal propagation, whereas lateral propagation was marked by significant horizontal deviation of the extrusion point ($\Pi_5 > 0.4$, Table 3 and Figure 12). A main difference between the experiments and the *Pinel and Jaupart* [2000, 2004b] predictions is that GS, after stalling, always reached the surface because of maintained overpressure, whereas in numerical models, magma which had insufficient pressure to propagate laterally was stored below the volcano.

[49] Figures 12b–12c show that it is only for dykes with limited relative overpressure (low Π_{11} value) rising under steep cones that edifice-induced load is dominant and forces the intrusion to propagate laterally. For a higher relative overpressure, magma tends to form reservoir-like features that enable the intrusion to build up sufficient pressure to still propagate in the central part of the edifice, if cone slope is not too high. For low-angle cones, dykes can erupt through the central part of the edifice without a storage phase. These observations are consistent with relationships proposed by *Pinel and Jaupart* [2004b, Figure 12a], except that magma stalling at shallow level was the typical behavior of low dyke overpressure (higher magma density) in their numerical model. Lateral propagation occurred for dykes with high overpressure (less dense magma) because intrusions were driven by buoyancy and could not develop into reservoirs where magma can accumulate and pressure can build up.

[50] Figures 12c–12d show that lateral dyke propagation is also constrained by the relative depth of dyke initiation (Π_2). Evidence of lateral propagation is observed for low values of Π_2, and thus deep initiation relative to cone size. If the source is shallow (high Π_2 value), the dyke will stall and finally extrude within the upper cone, if magma input is sufficient. This can be related to the general increase in dyke length for thicker crust. It suggests that in addition to the volcano load effect, the geometric effect of a dyke intersecting the surface at the cone base when initiated at great depth is also an important constraint for eruption outbreak location, as suggested by numerical modeling by *Gaffney and Damjanac* [2006].

[51] A decrease in dyke ascent velocity was observed in gelatin models as the dyke tip approached within 0.8–1.5 cone radius below the cone. This is consistent with numerical predictions of a marked propagation rate drop due to the compressive stress generated by edifice load [*Pinel and Jaupart*, 2000; *Watanabe et al.*, 2002] when magma reaches a depth equal to the volcano radius. This decrease in vertical ascent velocity could not be directly observed in the sand-box experiments, but can be extrapolated from observations of a corresponding level of greater horizontal extension for the intrusions.

5.2. Limitations of Experiments and Additional Key Factors

[52] Analogue experiments enable visualization and analysis of a simplified representation of a natural system. In addition to the inherent randomness of experimental results, several limitations of the analogue models can be highlighted. First, some components of natural volcanic systems are not accounted for in our analogue experiments. Experiments with a pre-established conduit up to the cone base showed that an established magmatic system (i.e., magma chamber, conduits, former intrusions) existing below and within volcanoes reduces the cone load control upon magma propagation. In the natural cases, this factor can account for the occurrence of most eruptions in the axial zones of natural volcanoes. A central conduit, or a central weak zone, through which successive intrusions preferentially propagate, generally characterizes volcanoes with regular eruptions, i.e., volcanoes where dyke ascent timescale is smaller or equal to dyke cooling or closure timescales, which themselves depend on dyke width and driving overpressure, in turn dependent on the magma rheology and supply rate.

[53] Second, volcano load and regular magma intrusion can favor the formation of shallow magma chambers in which magma can evolve [*van Wyk de Vries and Borgia*, 1996; *Pinel and Jaupart*, 2000; *Muller et al.*, 2001; *Borgia and van Wyk de Vries*, 2003]. Analogue experiments presented here are only valid for vertical dykes rising from depth (i.e., a deep reservoir) in the volcano axial zone without intersecting any pre-existing shallow chambers. This is the case for volcanoes with a long repose time, or for magmas rising at the system periphery [e.g., Etna 2000, *Acocella and Neri*, 2003], bypassing shallow chambers. Numerical models by *Pinel and Jaupart* [2003] for dyke nucleation from a pressurized magma chamber under a

Figure 12. Relationships between experimental dimensionless numbers and the type of interaction between cone load and ascending intrusions. (a) Graphical sketch of the relationships obtained from the numerical modeling of dykes ascending from a deep source underneath a cone with a fixed slope [after *Pinel and Jaupart*, 2004b]; (b) dyke behavior in sand-box experiments for varying cone slope (Π_1) and relative intrusion overpressure (Π_{11}); (c) schematic summary of dyke behavior in function of Π_1 and Π_{11}; (d) dyke behavior in sand-box experiments for varying cone slope (Π_1) versus cone size relative to crust thickness (Π_2); (e) schematic summary of dyke behavior in function of Π_1 and Π_2. Note that Figures 12c and 12e are merely illustrating the likely, or dominant, behavior of dyke propagation for contrasting experimental conditions. Significant overlap is observed between these fields in the experimental results. This overlap is attributed to the inherent variability in the experiments.

volcano load resulted in vertical dykes rising below the cone summit, but shallow magma chamber inflation can also nucleate inclined dyke sheets [*Gudmunsson*, 2006; *Cañon-Tapia and Merle*, 2006]. These studies suggest that the shape of magma chambers can influence the original location and orientation of dykes, although volcano load was not accounted for in these models. Dyke nucleation at shallow level and presence of a shallow magma reservoir

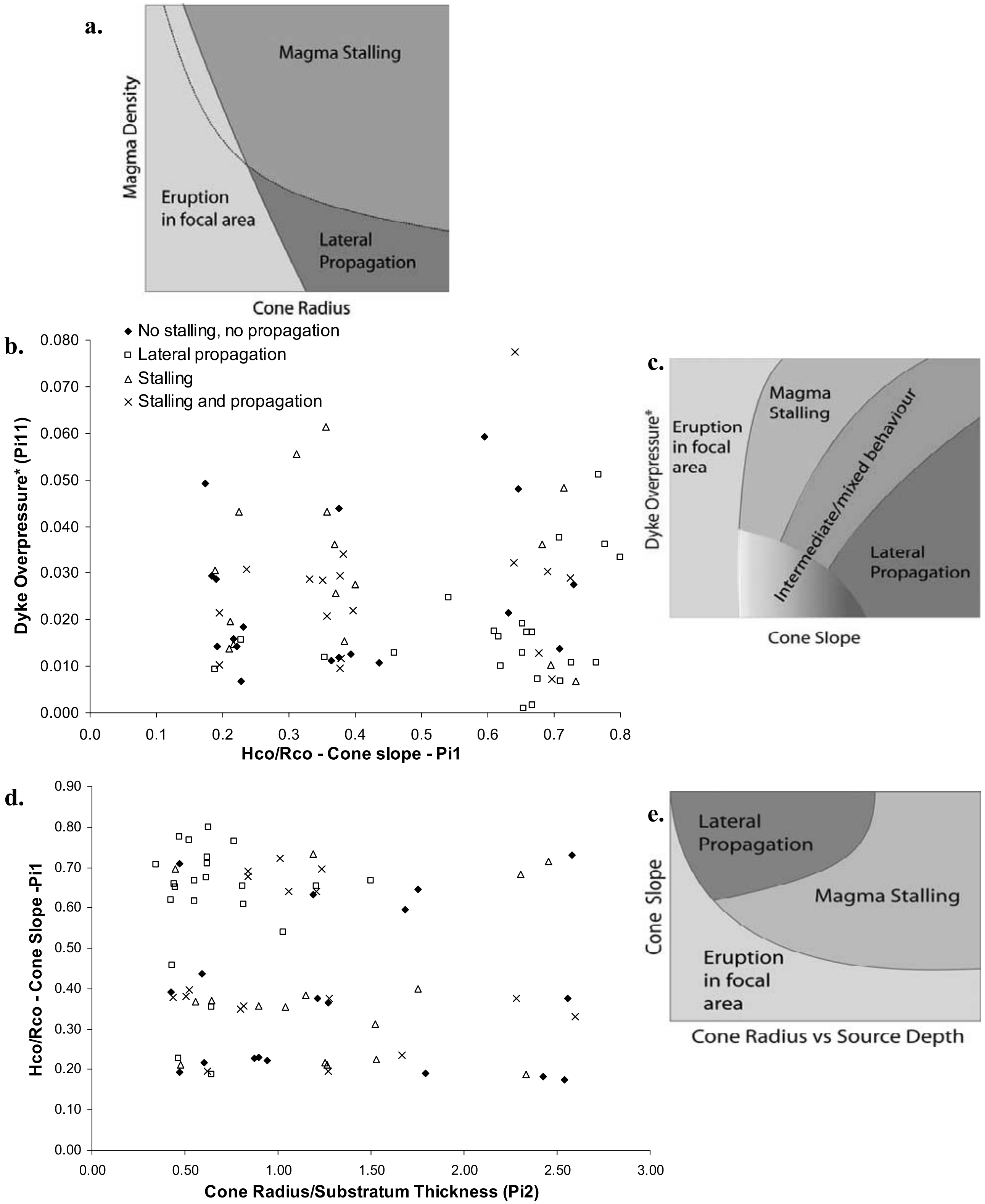

Figure 12

are expected to reduce the cone load control upon the extrusion point location [*Dumaisnil*, 2007].

[54] Third, the analogue models were made using homogeneous media to remove the complication of lithological boundaries and of material with contrasted rheological properties, in order to isolate the effect of loading. In nature, the crust through which intrusions propagate is a heterogeneous medium made up of layers with contrasting mechanical properties (i.e., sediments, lava flows, pyroclastics). It has been argued that most rising dykes get arrested because of strong variations in the Young's modulus of the layers in or directly below volcanic edifices [*Gudmunsson and Philipp*, 2006]. Experiments on dyke propagation in layered gelatin with contrasting fracture toughness (or Young's modulus) suggested that a dyke can turn into a sill or laccolith at or directly below rheological boundaries [*Hyndman and Alt*, 1987; *Rivalta et al.*, 2005; *Kavanagh et al.*, 2006]. The volcano base or BIS discussed in our models might correspond to a lithological boundary at natural volcanoes, different types of deposits having contrasting characteristic slopes. It has been shown that these rheological boundaries can enhance lateral intrusion propagation away from the volcano's axial zone [*Pinel and Jaupart*, 2004b]. Crust heterogeneity could be modeled in sand-box experiments using silicone layers [*Mathieu and van Wyk de Vries*, 2009] or granular layers of contrasting density and/or cohesion.

[55] Fourth, volcanoes are dynamic entities that grow with eruption or with magma intrusions, and whose morphology is also affected by interaction with their substratum or with tectonic structures. Volcano spreading due to an underlying weak sediment layer causes extensional grabens to form. Extension can favor magma rise through the volcano core. Regional tectonic structures can also control vent orientation and spatial distribution, especially on lower flanks.

[56] Fifth, intrusion rates, ascent velocity and overpressure are expected to vary greatly for natural dykes. In our experiments, intrusion rate and dyke overpressure were varied by one and two orders of magnitude, respectively, as a preliminary sensitivity analysis. The modeled intrusion rates approach the highest intrusion rates expected in natural cases. Results suggest that lower intrusion rates, associated with lower dyke overpressure, will tend to increase the topographic effect on the stress balance. Specific sets of experiments allowing for greater variations in intrusion rate or dyke overpressure should be developed in the future to quantitatively constrain the effect of these parameters on the lateral propagation of intrusions.

5.3. Conceptual Model and Applications

[57] Controls on vent location and dyke propagation evolve through the evolution of a volcanic edifice. The following conceptual model can be proposed (Figure 13a), specifically for vent distribution at stratovolcanoes or continental shields. Repetitive magma input from a deep source and the increasing compressive stress caused by the growing volcano will favor magma reservoir formation in the upper crust below the volcano axial zone [*van Wyk de Vries and Borgia*, 1996; *Borgia et al.*, 2000; *Pinel and Jaupart*, 2000; *Muller et al.*, 2001; *Borgia and van Wyk de Vries*, 2003]. As long as the central conduit remains open, magma chamber overpressure is released by central eruptions. Volcano growth above a given height might cause sufficient compressive stress to keep the conduit closed most of the time and prevent regular central eruptions. Magma will stall in the magma chamber and eruptions will occur at the volcano periphery, through lateral dyke intrusion from the chamber or from the remaining part of the conduit (Figure 13a). The magma reservoir will enlarge and allow magma differentiation, decrease in magma density and volatile accumulation.

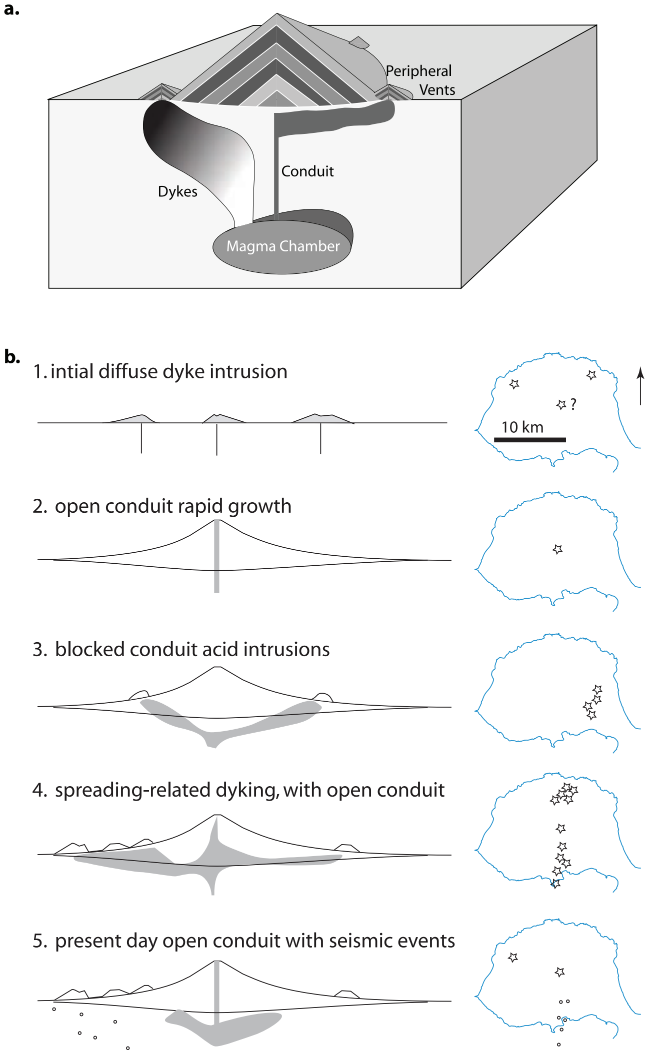

Figure 13. (a) Conceptual model for the relationship between dyke propagation and vent distribution. Volcano load prevents central eruption; dykes propagate laterally from the conduit or directly from the magma chamber and cause eruptions at cone base; (b) eruptive history of Concepción volcano, Nicaragua presented in section and map sketches, adapted from the works of *Borgia and van Wyk de Vries* [2003] and *van Wyk de Vries* [1993]. Vent (white stars) opening away from the volcano summit characterizes most of the evolution of Concepción.

[58] As a volcano grows, it will start to spread if it is located on a thin ductile substratum. Spreading is associated with edifice extension. Magma rise will then be favored along radial rift zones within the volcano cone. For resistant constructs or constructs located on thick ductile substratum, volcano growth will be associated with edifice sagging into the substratum rather than with spreading [*van Wyk de Vries and Matela*, 1998]. This process, sometimes associated with extrusion of the ductile substratum (i.e., sediments) at the volcano periphery, will have a different impact on vent distribution, probably favoring eruptions at the system periphery.

[59] This model is consistent with the evolution of the vent distribution at Concepción volcano, Nicaragua (Figure 13b) [*van Wyk de Vries*, 1993; *Borgia and van Wyk de Vries*, 2003]. Five stages of volcano growth and eruptive history can be discriminated: (1) an initial stage, when dykes of basaltic magma rose to erupt without any edifice present; (2) a growth stage when eruptions became focused on a central conduit and a cone rapidly grew; (3) a compression phase, when the volcano flexed into the substratum, with thrusting occurring at the base because of constriction, and acid domes being emplaced around the base; (4) a spreading phase when the volcano was cut by a rift and basic magma was erupted from the base and summit, with a concentration around the BIS; (5) present day activity when an open conduit channels magmas to the summit and when seismicity is concentrated at the southern base of the volcano, suggesting continued intrusion in this area (Figure 13b). Note that eruptions at the base of Concepción characterize all phases of activity after the initial growth of the stratovolcano.

[60] Development of peripheral vents might thus especially occur at a stage when the volcano is sufficiently big to exert a significant load on its substratum. This occurs before the volcano starts spreading, or for nonspreading volcanoes. The proposed model is valid for stratovolcanoes fed from deep sources. If dyke orientation is controlled by tectonic structures, vents will concentrate at specific cone base regions and will lead to the formation of an elongated volcano.

[61] There are few studies documenting the propagation path or flow velocity for single eruptive dykes. Using seismic data, *Peltier et al.* [2005] analyzed the velocity and direction of dyke propagation from a shallow reservoir ~3 km below the surface for eruptive events that occurred between 1998 and 2004 at Piton de la Fournaise (Réunion Island). These authors described a shift from rapid vertical ascent (~2 m/s) to slower (0.2–0.8 m/s) lateral propagation as the dyke reached the Dolomieu cone base. This directional change was attributed to the presence of fractured rift zones, but it can also be interpreted as resulting from dyke reorientation caused by cone load stresses [*Peltier et al.*, 2005]. Lateral dyke propagation was also found as the best-fit model accounting for deformation and earthquakes associated with the March 1998 eruption at Piton de la Fournaise, characterized by two main eruptive sites, namely at the N and WSW base of the Dolomieu cone [*Battaglia and Bachèlery*, 2003].

[62] Field observations also provide evidence for lateral dyke propagation and for extrusion focusing at a BIS. For example, this is illustrated in the study of radial dykes at Summer Coon volcano (Colorado, USA [*Poland et al.*, 2008]). This study focused on silicic dykes, those being much longer than basaltic ones observed in the field. The observation of dykes of increasing thickness toward the periphery of this eroded stratovolcano led these authors to suggest that most of the voluminous eruptions from radial dykes occurred at the lower flanks. *Poland et al.* [2008] attributed magma horizontal propagation at the volcano base either to a neutral buoyancy level or to a stress barrier generated by a lithological contrast or by the volcano load. This field case shows that cone load, while acting concomitantly with other factors favoring lateral propagation (i.e., lithological boundaries), can be a significant process even for lower density, silicic intrusions at stratovolcanoes.

[63] At many volcanoes, peripheral vent products have a more primitive magmatic composition than the magma erupted centrally, although contrasted compositions might be erupted simultaneously. One possible explanation involves stratified magma chambers. Another possible explanation, based on the “shadow zone” concept (i.e., the zone where no peripheral vents occur around a central eruption site) is that primitive magma occurring at the periphery rises directly from a deep source, whereas magma erupting centrally is integrated in shallow chambers that need to differentiate to build up a sufficient buoyancy force to erupt centrally [*Pinel and Jaupart*, 2004b]. This spatial variation in magma composition is also consistent with the results of our experiments. Mafic dykes are expected to rise with lower overpressure (i.e., as the density contrast is smaller) and from a deeper source. Hence they are more likely to be affected by the volcano load.

6. Conclusions

[64] Remote sensing observations of vent distribution and analogue experiments results show that dykes with limited overpressure rising from a deep reservoir are expected to reorientate underneath a steep volcanic cone in response to the local, edifice-induced, stress field, if no established conduit or extensional processes favor magma propagation in the axial zone. Volcano load prevents vertical dyke propagation and favors lateral propagation, causing eruptions to occur close to the volcano base. Vents at and beyond a marked BIS have been observed for volcanic edifices on different scales, from scoria cones to broad oceanic shields. Figure 14 illustrates the range of Π_1 and Π_2 values for different types of volcanoes and for specific examples presented in this paper.

[65] Most field studies of subvolcanic intrusive complexes have so far not been able to render the 3D shape of the plumbing system because of the 2D nature of outcrops. Analogue experiments provide valuable insights into the 3D plumbing shape of subvolcanic complexes suggesting more complex intrusion shapes and interactions between intrusive bodies (sill/dyke) than previously thought [e.g., *Emeleus and Bell*, 2005]. Primary results presented here and by *Mathieu et al.* [2008] closely match available geological evidence. The predictions from the experiments may motivate renewed efforts to record the 3D morphology of volcano plumbing systems in the field [e.g., *Di Stefano*

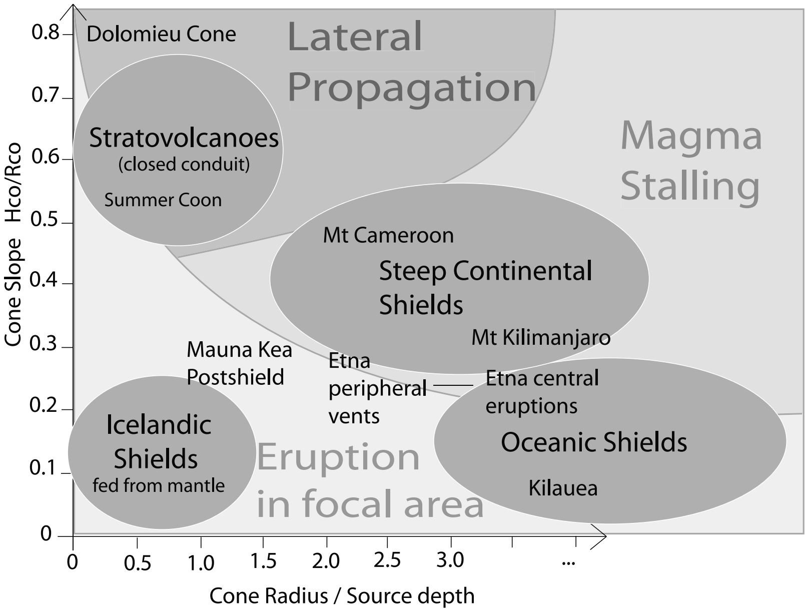

Figure 14. Sketch of the range of Π_1 and Π_2 values for different types of volcanoes and specific examples discussed in the text. Comparison with Figure 12e enables to see that volcanoes plotting in the upper left corner of the graph are the most susceptible to load-induced dyke lateral propagation.

and Chiarabba, 2002]. It may also help geophysicists to invert ground deformation, seismic or gas emission data related to magma emplacement/eruption and associated with complex plumbing.

[66] **Acknowledgments.** M.K. and G.G.J.E. are supported by the Belgian Research Foundation (FWO-Vlaanderen). M.K. also thanks the FWO and the "Fondation Belge de la Vocation" for funding his visits to LMV. We thank Tate & Lyle for providing the Golden syrup at LMV. Authors are grateful to T. Walter for insightful discussions on analogue experiments. This paper is dedicated to George Walker, who pioneered the first analogue experiments of the type discussed here, and in so doing inspired the present work.

References

Acocella, V., and M. Neri (2003), What makes flank eruptions? The 2001 Etna eruption and its possible triggering mechanisms, *Bull. Volcanol.*, *65*, 517–529.

Annen, C., J.-F. Lénat, and A. Provost (2001), The long-term growth of volcanic edifices: Numerical modelling of dyke intrusion and lava-flow emplacement, *J. Volcanol. Geotherm. Res.*, *105*, 263–289.

Bacon, C. R. (1985), Implications of silicic vent patterns for the presence of large crustal magma chambers, *J. Geophys. Res.*, *90*, 11,243–11,252.

Battaglia, J., and P. Bachèlery (2003), Dynamic dyke propagation deduced from tilt variations preceding the March 9, 1998, eruption of the Piton de la Fournaise volcano, *J. Volcanol. Geotherm. Res.*, *120*, 289–310.

Battaglia, J., K. Aki, and T. Staudacher (2005), Location of tremor sources and estimation of lava output using tremor source amplitude on the Piton de la Fournaise volcano. part II: Estimation of lava output, *J. Volcanol. Geotherm. Res.*, *147*, 291–308.

Behncke, B., M. Neri, E. Pecora, and V. Zanon (2006), The exceptional activity and growth of the Southeast Crater, Mount Etna (Italy), between 1996 and 2001, *Bull. Volcanol.*, *69*, 149–173.

Borgia, A., and B. van Wyk de Vries (2003), The volcano-tectonic evolution of Concepción, Nicaragua, *Bull. Volcanol.*, *65*, 248–266.

Borgia, A., C. Poore, M. J. Carr, W. G. Melson, and G. E. Alvarado (1988), Structural, stratigraphic, and petrologic aspects of the Arenal-Chato volcanic system, Costa Rica: Evolution of a young stratovolcanic complex, *Bull. Volcanol.*, *50*, 86–105.

Borgia, A., P. T. Delaney, and R. P. Denlinger (2000), Spreading volcanoes, *Annu. Rev. Earth Planet. Sci.*, *28*, 539–570.

Cañon-Tapia, E., and O. Merle (2006), Dike nucleation and early growth from pressurized magma chambers: Insights from analogue models, *J. Volcanol. Geotherm. Res.*, *158*, 207–220.

Carr, M. J. (1984), Symmetrical and segmented variation of physical and geochemical characteristics of the Central American volcanic front, *J. Volcanol. Geotherm. Res.*, *20*, 231–252.

Carr, M. J., and N. K. Pontier (1981), Evolution of a young parasitic cone towards a mature central vent: Izalco and Santa Ana volcanoes in El Salvador, Central America, *J. Volcanol. Geotherm. Res.*, *11*, 277–292.

Chadwick, W. W., and J. H. Dietrich (1995), Mechanical modeling of circumferential and radial dike intrusion on Galapagos volcanoes, *J. Volcanol. Geotherm. Res.*, *66*, 37–52.

Connor, C. B., C. D. Condit, L. S. Crumpler, and J. C. Aubele (1992), Evidence of regional structural controls on vent distribution: Springerville Volcanic Field, Arizona, *J. Geophys. Res.*, *97*, 12,349–12,359.

Corazzato, C., and A. Tibaldi (2006), Fracture control on type, morphology and distribution of parasitic volcanic cones: An example from Mt. Etna, Italy, *J. Volcanol. Geotherm. Res.*, *158*, 177–194.

Dahm, T. (2000), Numerical simulations of the propagation path and the arrest of fluid-filled fractures in the Earth, *Geophys. J. Int.*, *141*, 623–638.

Decker, R. W. (1987), Dynamics of Hawaiian volcanoes: An overview, *U.S. Geol. Surv. Prof. Pap.*, *1350*, 997–1018.

Dieterich, J. H. (1988), Growth and persistence of Hawaiian volcanic rift zones, *J. Geophys. Res.*, *93*, 4258–4270.

Di Stefano, R., and C. Chiarabba (2002), Active source tomography at Mt. Vesuvius: Constraints for the magmatic system, *J. Geophys. Res.*, *107*(B11), 2278, doi:10.1029/2001JB000792.

Donnadieu, F., and O. Merle (1998), Experiments on the indentation process during cryptodome intrusions: New insights into Mount St. Helens deformation, *Geology*, *26*, 79–82.

Dumaisnil, C. (2007), Modélisation analogique d'intrusions magmatiques superficielles à l'intérieur d'un édifice volcanique, M.Sc. thesis, 50 pp., Université Blaise-Pascal, Clermont Ferrand, France.

Emeleus, C. G., and B. R. Bell (2005), *British Regional Geology: The Palaeogene Volcanic Districts of Scotland*, 4th ed., 213 pp., British Geol. Surv., Nottingham, U. K.

Fialko, Y. A., and A. M. Rubin (1999), What controls the along-strike slopes of volcanic rift zones?, *J. Geophys. Res.*, *104*, 20,007–20,020.

Francis, P., and C. Oppenheimer (2003), *Volcanoes*, 2nd ed., 534 pp., Oxford Univ. Press, New York.

Gaffney, E. S., and B. Damjanac (2006), Localization of volcanic activity: Topographic effects on dike propagation, eruption and conduit formation, *Geophys. Res. Lett.*, *33*, L14313, doi:10.1029/2006GL026852.

Galland, O., P. R. Cobbold, J. de Bremond d'Ars, and E. Hallot (2007), Rise and emplacement of magma during horizontal shortening of the brittle crust: Insights from experimental modeling, *J. Geophys. Res.*, *112*, B06402, doi:10.1029/2006JB004604.

Gudmundsson, A. (2002), Emplacement and arrest of sheets and dykes in central volcanoes, *J. Volcanol. Geotherm. Res.*, *116*, 279–298.

Gudmunsson, A. (2006), How local stresses control magma-chamber ruptures, dyke injections, and eruption in composite volcanoes, *Earth Sci. Rev.*, *79*, 1–31.

Gudmunsson, A., and S. L. Philipp (2006), How local stress fields prevent volcanic eruptions, *J. Volcanol. Geotherm. Res.*, *158*, 257–268.

Hildreth, W., and J. Fierstein (1997), Recent eruptions of Mount Adams, Washington, Cascades, USA, *Bull. Volcanol.*, *58*, 472–490.

Hildreth, W., and J. Fierstein (2000), The Katmai volcanic cluster and the great eruption of 1912, *Geol. Soc. Am. Bull.*, *112*, 1594–1620.

Hyndman, D. W., and D. Alt (1987), Radial dikes, laccoliths, and gelatin models, *J. Geol.*, *95*, 763–774.

Jaeger, J. C., and N. G. W. Cook (1971), *Fundamentals of Rock Mechanics*, 585 pp., CRC Press, Boca Raton, Fla.

Johnson, A. M. (1970), *Physical Processes in Geology*, 794 pp., W.H. Freeman, New York.

Kaneko, T., A. Yasuda, T. Shimano, S. Nakada, T. Fujii, T. Kanazawa, A. Nishizawa, and Y. Matsumoto (2005), Submarine flank eruption preceding caldera subsidence during the 2000 eruption of Miyakejima volcano, Japan, *Bull. Volcanol.*, *67*, 243–253.

Kavanagh, J. L., T. Menand, and R. S. J. Sparks (2006), An experimental investigation of sill formation and propagation in layered elastic media, *Earth Planet. Sci. Lett.*, *245*, 799–813.

Kervyn, M., G. G. J. Ernst, J. Klaudius, J. Keller, E. Mbede, and P. Jacobs (2008), Remote sensing evidence of sector collapses and debris avalanches at Oldoinyo Lengai and Kerimasi volcanoes, Tanzania, *Int. J. Remote Sens.*, *29*, 6565–6595.

Klausen, M. B. (2006), Geometry and mode of emplacement of dike swarms around the Birnudalstindur igneous centre, SE Iceland, *J. Volcanol. Geotherm. Res.*, *151*, 340–356.

Luhr, J. F., and T. Simkin (1993), *Parícutin: The Volcano Born in a Mexican Cornfield*, 427 pp., Geoscience Press, Phoenix, Ariz.

Mac Donald, G. A. (1945), Ring structures at Mauna Kea, Hawaii, *Am. J. Sci.*, *243*, 210–217.

Mathieu, L., and B. van Wyk de Vries (2009), Edifice and substrata deformation induced by intrusive complexes and gravitational loading in the Mull volcano (Scotland), *Bull. Volcanol.*, in press.

Mathieu, L., B. van Wyk de Vries, E. Holohan, and V. R. Troll (2008), Dykes, cups, saucers and sills: Analogue experiments on magma intrusion into brittle rocks, *Earth Planet. Sci. Lett.*, *271*, 1–13.

Mazzarini, F., and M. D'Orazio (2003), Spatial distribution of cones and satellite-detected lineaments in the Pali Aike Volcanic Field (Southernmost Patagonia): Insights into the tectonic setting of a Neogene rift system, *J. Volcanol. Geotherm. Res.*, *125*, 291–305.

McGuire, W. J., and A. D. Pullen (1989), Location and orientation of eruptive fissures and feeder-dikes at Mount Etna—Influence of gravitational and regional tectonic stress regimes, *J. Volcanol. Geotherm. Res.*, *38*, 325–344.

McNight, S. B. (1995), Geology and petrology of Cerro Negro volcano, Nicaragua, M.Sc. thesis, 130 pp., Arizona State Univ, Tempe, Ariz.

Menand, T. (2008), The mechanics and dynamics of sills in layered elastic rocks and their implications for the growth of laccoliths and other igneous complexes, *Earth Planet. Sci. Lett.*, *267*, 93–99.

Menand, T., and S. R. Tait (2002), The propagation of a buoyant liquid-filled fissure from a source under constant pressure: An experimental approach, *J. Geophys. Res.*, *107*(B11), 2306, doi:10.1029/2001JB000589.

Merle, O., and A. Borgia (1996), Scaled experiments of volcanic spreading, *J. Geophys. Res.*, *101*, 13,805–13,817.

Middleton, G. V., and P. R. Wilcock (1994), *Mechanics in the Earth and Environmental Sciences*, 459 pp., Cambridge Univ. Press, New York.

Moore, J. G., and D. A. Clague (1992), Volcano growth and evolution of the island of Hawaii, *Geol. Soc. Am. Bull.*, *104*, 1471–1484.

Muller, J. R., G. Ito, and S. J. Martel (2001), Effects of volcano loading on dike propagation in an elastic half-space, *J. Geophys. Res.*, *106*, 11,101–11,113.

Murdoch, L. C. (1993a), Hydraulic fracturing of soil during laboratory experiments. part I: Methods and observations, *Géotechnique*, *43*, 255–265.

Murdoch, L. C. (1993b), Hydraulic fracturing of soil during laboratory experiments. part II: Propagation, *Géotechnique*, *43*, 266–276.

Murdoch, L. C. (1993c), Hydraulic fracturing of soil during laboratory experiments. part III: Theoretical analysis, *Géotechnique*, *43*, 277–287.

Naranjo, J. A., R. S. J. Sparks, M. V. Stasiuk, H. Moreno, and G. J. Ablay (1992), Morphological, structural and textural variations in the 1988–1990 andesite lava of Lonquimay volcano, Chile, *Geol. Mag.*, *129*, 657–678.

Naumann, T., and D. Geist (2000), Physical volcanology and structural development of Cerro Azul Volcano, Isabela Island, Galapagos: Implications for the development of Galapagos-type shield volcanoes, *Bull. Volcanol.*, *61*, 497–514.

Peltier, A., V. Ferrazzini, T. Staudacher, and P. Bachèlery (2005), Imaging the dynamics of dyke propagation prior to the 2000–2003 flank eruptions at Piton de La Fournaise, Reunion Island, *Geophys. Res. Lett.*, *32*, L22302, doi:10.1029/2005GL023720.

Pinel, V., and C. Jaupart (2000), The effect of edifice load on magma ascent beneath a volcano, *Philos. Trans. R. Soc. London*, *358*, 1515–1532.

Pinel, V., and C. Jaupart (2003), Magma chamber behavior beneath a volcanic edifice, *J. Geophys. Res.*, *108*(B2), 2072, doi:10.1029/2002JB001751.

Pinel, V., and C. Jaupart (2004a), Likelihood of basaltic eruptions as a function of volatile content and volcanic edifice size, *J. Volcanol. Geotherm. Res.*, *137*, 201–217.

Pinel, V., and C. Jaupart (2004b), Magma storage and horizontal dyke injection beneath a volcanic edifice, *Earth Planet. Sci. Lett.*, *221*, 245–262.

Poland, M. P., W. P. Moats, and J. H. Fink (2008), A model for radial dike emplacement in composite cones based on observations from Summer Coon volcano, Colorado, USA, *Bull. Volcanol.*, *70*, 861–875, doi:810.1007/s00445-00007-00175-00449.

Pollard, D. D. (1973), Derivation and evaluation of a mechanical model for sheet intrusions, *Tectonophysics*, *19*, 233–269.

Pollard, D. D. (1987), Elementary fracture mechanics applied to the structural interpretation of dikes, in *Mafic Dyke Swarms*, *Spec. Pap.*, edited by H. C. Halls and W. F. Fahrig, pp. 5–24, Geol. Assoc. of Canada.

Porter, S. C. (1972), Distribution, morphology and size frequency of cinder cones on Mauna Kea volcano, Hawaii, *Geol. Soc. Am. Bull.*, *83*, 3607–3612.

Ramberg, H. (1981), *Gravity, Deformation and the Earth's Crust*, 452 pp., Elsevier, New York.

Rivalta, E., and T. Dahm (2006), Acceleration of buoyancy-driven fractures and magmatic dikes beneath the free surface, *Geophys. J. Int.*, *166*, 1424–1439.

Rivalta, E., M. Bottinger, and T. Dahm (2005), Buoyancy-driven fracture ascent: Experiments in layered gelatine, *J. Volcanol. Geotherm. Res.*, *144*, 273–285.

Rowland, S. K., and H. Garbeil (2000), The slopes of oceanic basalt volcanoes, in *Remote Sensing of Active Volcanism*, *Geophys. Monogr. Ser.*, vol. 116, edited by P. J. Mouginis-Mark et al., pp. 223–247, AGU, Washington, D. C.

Shteynberg, G. S., and T. S. V. Solovyev (1976), The shape of volcanoes and the position of subordinate vents, *Earth Phys.*, *5*, 83–84.

Simkin, T., and L. Siebert (1994), *Volcanoes of the World*, 2nd ed., 349 pp., Geosciences Press, Tucson, Ariz.

Spera, F. J. (2000), Physical properties of magma, in *Encyclopedia of Volcanoes*, edited by H. Sigurdsson et al., pp. 171–190, Elsevier, New York.

Suh, C. E., R. S. J. Sparks, J. G. Fitton, S. N. Ayonghe, C. Annen, R. Nana, and A. Luckman (2003), The 1999 and 2000 eruptions of Mount Cameroon: Eruption behaviour and petrochemistry of lava, *Bull. Volcanol.*, *65*, 267–281.

Takada, A. (1990), Experimental study on propagation of liquid-filled crack in gelatin: Shape and velocity in hydrostatic stress condition, *J. Geophys. Res.*, *95*, 8471–8481.

Thomson, K. (2007), Determining magma flow in sills, dykes and laccoliths and their implications for sill emplacement mechanisms, *Bull. Volcanol.*, *70*, 183–201.

Valentine, G. A., and G. N. Keating (2007), Eruptive styles and inferences about plumbing systems at Hidden Cone and Little Black Peak scoria cone volcanoes (Nevada, U.S.A.), *Bull. Volcanol.*, *70*, 105–113.

Valentine, G. A., and K. E. C. Krogh (2006), Emplacement of shallow dikes and sills beneath a small basalt volcanic center—The role of pre-existing structure (Paiute ridge, southern Nevada, USA), *Earth Planet. Sci. Lett.*, *246*, 217–230.

van Wyk de Vries, B. (1993), Tectonics and magma evolution of Nicaraguan volcanic systems, Ph.D. thesis, 328 pp., Earth Sciences Dept., Open University, Milton Keynes, U. K.

van Wyk de Vries, B., and A. Borgia (1996), The role of basement in volcano deformation, in *Volcano Instability on the Earth and other Planets*, edited by W. J. McGuire et al., *Geol. Soc. London Spec. Publ.*, 110, 95–110.

van Wyk de Vries, B., and R. Matela (1998), Styles of volcano-induced deformation: Numerical models of substratum flexure, spreading and extrusion, *J. Volcanol. Geotherm. Res.*, *81*, 1–18.

Walker, G. P. L. (1990), Geology and volcanology of the Hawaiian Islands, *Pac. Sci.*, *44*, 315–347.

Walker, G. P. L. (1993), Re-evaluation of inclined intrusive sheets and dykes in the Cuillins volcano, Isle of Skye, in *Magmatic Processes and Plate Tectonics*, edited by H. M. Prichard et al., *Geol. Soc. London Spec. Publ.*, 76, 489–497.

Walker, G. P. L. (1995), Congruent dyke-widths in large basaltic volcanoes, in *Physics and Chemistry of Dykes*, edited by G. Baer and A. Heimann, pp. 35–40, A. A. Balkema, Brookfield, Vt.

Walker, G. P. L. (1999), Volcanic rift zones and their intrusion swarms, *J. Volcanol. Geotherm. Res.*, *94*, 21–34.

Walter, T., and V. R. Troll (2003), Experiments on rift zone evolution in unstable volcanic edifices, *J. Volcanol. Geotherm. Res.*, *127*, 107–120.

Walter, T., and F. Amelung (2006), Volcano-earthquake interaction at Mauna Loa volcano, Hawaii, *J. Geophys. Res.*, *111*, B08301, doi:10.1029/2005JB003861.

Watanabe, T., T. Masuyama, K. Nagaoka, and T. Tahara (2002), Analog experiments on magma-filled cracks: Competition between external stresses and internal pressure, *Earth Planets Space*, *54*, 1247–1261.

G. G. J. Ernst, P. Jacobs, and M. Kervyn, Mercator and Ortelius Research Centre for Eruption Dynamics, Department of Geology and Soil Sciences, Ghent University, Krijgslaan 281/S8, B-9000 Gent, Belgium. (matthieu.kervyndemeerendre@ugent.be)

L. Mathieu and B. van Wyk de Vries, Laboratoire Magma et Volcans, Université Blaise Pascal, 5 Rue Kessler, FR-63038 Clermont-Ferrand, France.